BBA - Molecular and Cell Biology of Lipids 1866 (2021) 158890

Contents lists available at ScienceDirect

BBA - Molecular and Cell Biology of Lipids

journal homepage: www.elsevier.com/locate/bbalip

Nanoscale mapping of nuclear phosphatidylinositol phosphate landscape by dual-color dSTORM

Peter Hoboth [a], Martin Sztacho [a], Ondřej Šebesta [b], Martin Schätz [b], Enrique Castano [a,c], Pavel Hozák [a,d,e,*]

[a] Department of Biology of the Cell Nucleus, Institute of Molecular Genetics of the Czech Academy of Sciences, Vídeňská 1083, 142 20 Prague, Czech Republic
[b] Faculty of Science, Charles University, Albertov 6, 128 00 Prague, Czech Republic
[c] Biochemistry and Molecular Plant Biology Department, Centro de Investigación Científica de Yucatán, A.C. Calle 43 No. 130, Colonia Chuburná de Hidalgo, Mérida C. P. 97200, Yucatán, Mexico
[d] Department of Epigenetics of the Cell Nucleus, Institute of Molecular Genetics of the Czech Academy of Sciences, division BIOCEV, Průmyslová 595, 252 20 Vestec, Czech Republic
[e] Microscopy Centre, Institute of Molecular Genetics of the Czech Academy of Sciences, Vídeňská 1083, 142 20 Prague, Czech Republic

ARTICLE INFO

Keywords:
Cell nucleus
Nuclear speckles
Nucleolus
RNA polymerase II
Phosphatidylinositol phosphates
STORM

ABSTRACT

Current models of gene expression, which are based on single-molecule localization microscopy, acknowledge protein clustering and the formation of transcriptional condensates as a driving force of gene expression. However, these models largely omit the role of nuclear lipids and amongst them nuclear phosphatidylinositol phosphates (PIPs) in particular. Moreover, the precise distribution of nuclear PIPs in the functional sub-nuclear domains remains elusive. The direct stochastic optical reconstruction microscopy (dSTORM) provides an unprecedented resolution in biological imaging. Therefore, its use for imaging in the densely crowded cell nucleus is desired but also challenging. Here we present a dual-color dSTORM imaging and image analysis of nuclear PI(4,5)P2, PI(3,4)P2 and PI(4)P distribution while preserving the context of nuclear architecture. In the nucleoplasm, PI(4,5)P2 and PI(3,4)P2 co-pattern in close proximity with the subset of RNA polymerase II foci. PI(4,5)P2 is surrounded by fibrillarin in the nucleoli and all three PIPs are dispersed within the matrix formed by the nuclear speckle protein SON. PI(4,5)P2 is the most abundant nuclear PIP, while PI(4)P is a precursor for the biosynthesis of PI(4,5)P2 and PI(3,4)P2. Therefore, our data are relevant for the understanding the roles of nuclear PIPs and provide further evidence for the model in which nuclear PIPs represent a localization signal for the formation of lipo-ribonucleoprotein hubs in the nucleus. The discussed experimental pipeline is applicable for further functional studies on the role of other nuclear PIPs in the regulation of gene expression and beyond.

1. Introduction

The eukaryotic cell is functionally compartmentalized into membrane-bound and membrane-less compartments. The eukaryotic nucleus is surrounded by the nuclear envelope, but the nuclear interior is membrane-less and displays a very complex functional architecture established and maintained by interactions between nucleic acids, proteins and lipids. Phosphatidylinositol phosphates (PIPs) control a wide range of biological processes from the plasma membrane to the nucleus [1,2]. Nuclear PIPs are found in addition to the nuclear envelope also in the nuclear interior where they are integral parts of membrane-less subcompartments [3–5]. Numerous nuclear proteins have the capacity to bind PIPs [6,7]. Moreover, nuclear PIPs, such as phosphatidylinositol 4,5-bisphosphate (PI(4,5)P2), regulate the enzymatic activity of nuclear proteins [8–13]. The nuclear PIP pool is largely independent of the PIP metabolism in the cytoplasm [1,14–16]. The inositol ring of PIPs can be reversibly phosphorylated at 3′, 4′, and 5′ positions generating 7 different phosphorylated species. Phosphatidylinositol 4-phosphate (PI(4)P) is phosphorylated either at position 3′ by enzyme PI3KCα [17] or at position 4′ by enzymes PIP5KIα and PIP5KIγ_i4 [9,18] to produce phosphatidylinositol 3,4-bisphosphate (PI(3,4)P2) or PI(4,5)P2, resp. Detergent-resistant nuclear PI(4)P and PI(4,5)P2 has been previously localized to the nuclear speckles, nucleoplasm and nucleoli by electron, conventional light and super-resolution microscopy [8,10,19–23].

* Corresponding author at: Department of Biology of the Cell Nucleus, Institute of Molecular Genetics of the Czech Academy of Sciences, Vídeňská 1083, 142 20 Prague, Czech Republic.
E-mail addresses: hozak@img.cas.cz, pavelhozak@gmail.com (P. Hozák).

https://doi.org/10.1016/j.bbalip.2021.158890
Received 2 September 2020; Received in revised form 10 January 2021; Accepted 22 January 2021
Available online 27 January 2021
1388-1981/© 2021 The Authors. Published by Elsevier B.V. This is an open access article under the CC BY-NC-ND license (http://creativecommons.org/licenses/by-nc-nd/4.0/).

Nuclear localization of PI(3,4)P2 has been previously reported [24,25] but the information about its sub-nuclear localization is missing. Interestingly, enzymes involved in the biosynthesis of PI(3,4)P2 and PI(4,5)P2 from PI(4)P, such as above mentioned PI3KCα, PIP5KIα and PIP5KIγ_i4 localize to the nuclear speckles [3,20,26], suggesting the role of nuclear speckles in the nuclear PIP metabolism.

Nuclear speckles, earlier referred to as interchromatin granule clusters [27], are nuclear sub-compartments enriched in the pre-mRNA splicing factors (SFs), such as SC35, small nuclear ribonucleoprotein particles (snRNPs) and poly(A)$^+$ RNAs [28–32]. Nuclear speckles were originally considered to be structural domains or storage sites for SFs. However, it is becoming increasingly evident that nuclear speckles are not just passive storage sites and the concept of a nuclear speckle periphery as a hub of active gene expression gains attention [33,34]. In line with this is the evidence that RNA polymerase II (RNAPII) was localized to the nuclear speckle periphery [35]. Nuclear speckles display a multilayered organization with SON, a scaffolding protein for pre-mRNA processing factors [36–38] and spliceosome associated factor SRRM2 at their core and RNAs at their periphery [39,40]. Additionally, nuclear speckles contain PI(4)P [19] and PI(4,5)P2, which has been suggested to directly or indirectly regulate the pre-mRNA splicing [7,20]. The shape of nuclear speckles reflects the transcriptional activity [34,41] and PI(4,5)P2 organization dynamically correlates with the nuclear speckle morphology [26]. Nevertheless, the role of PI(4,5)P2 and other PIPs, such as PI(4)P and PI(3,4)P2, in the nuclear speckles remain elusive. Therefore, here we quantitatively analyzed the nanoscale distribution of PI(4,5)P2, PI(3,4)P2 and PI(4)P with respect to the nuclear speckle marker SON.

An active cross-talk between nuclear speckles and nucleoplasm is in agreement with nuclear speckles being reservoirs of SFs as well as the places of active nuclear processes [42]. It has been suggested that an unknown nucleoplasmic body, independent of but related to the speckle periphery, represents a novel site of the regulation of gene expression [33]. PI(4,5)P2 has been earlier shown to localize with RNAPII in addition to the nuclear speckle markers [20]. We have shown that nucleoplasmic PI(4,5)P2 forms 40-100 nm foci that associate with the RNAPII transcription machinery [22]. We hypothesize that those nucleoplasmic PI(4,5)P2 foci serve as structural platforms, which facilitate the formation of RNAPII transcription factories and thereby participates in the formation of nuclear architecture competent for gene expression [5]. Therefore, here we analyzed in detail the spatial relationship of PI(4,5)P2 with RNAPII and extended our analyses also to PI(3,4)P2 and PI(4)P.

The nucleolus is the site of rRNA production and ribosomal subunits assembly and nucleolar architecture reflects its function [43,44]. The nucleolar fibrillar center (FC) is surrounded by the dense fibrillar component (DFC) and at the outer nucleolar layer is the granular component (GC). Synthesis of rRNA occurs at the FC/DFC border, the rRNA processing occurs sequentially at the DFC and GC. The latter is a site of ribosomal subunits assembly. During mitosis GC dissolves but components of FC and DFC, such as fibrillarin (Fib), concentrate into dozens of small droplets that fuse together in a process initiated by rDNA transcription to form functionally compartmentalized interphase nucleolus [45–47]. Nucleolar PI(4,5)P2 interacts with several proteins involved in the rDNA transcription, including UBF and Fib [10,11]. Fib is rRNA 2′-*O*-methyltransferase that localizes to the DFC [48]. Fib has also a ribonuclease activity, which is modulated by PI(4,5)P2 [8]. Therefore, we quantitatively characterized the spatial relationship between PI(4,5)P2 and Fib in nucleoli.

The eukaryotic nucleus has a very dense interior comprised of the viscoelastic polymer matrix. Therefore, due to the close packing, it is difficult to visualize its individual components with classical diffraction-limited light microscopy. Single-molecule localization microscopy (SMLM), such as direct stochastic optical reconstruction microscopy (dSTORM) [49,50] allows for the stochastic control in time of the emission of fluorophores. Therefore, due to the ability to resolve at nanoscale individual biomolecules, it provides the best imaging solution for dense and crowded environments such as cell nucleus [51–54]. SMLM methods provide also a new paradigm for the quantitative analysis of the relative nanoscale organization characterized by the spatial relationships between molecules. Co-localization can be thought of in the terms of correlation and co-occurrence [55,56]. The former represents a proportional co-distribution of two probes. The latter is the simple spatial overlap of the signals of two probes. The question of whether two probes co-distribute with each other can be answered at the level of individual molecules by coordinate-based co-localization, which allows to quantitatively assess the spatial relationship between two probes based on the nearest neighbor distances (NNDs) [57,58]. Alternatively, Coloc-Tesseler (CT) is a parameter-free co-localization analysis method based on the normalized Voronoi polygons surrounding individual molecules [59]. CT enables the quantitative evaluation of the spatial relationship between overlapping Voronoi polygons by Spearman and Manders coefficients. Spearman rank correlation coefficient is a non-parametric (non-linear) correlation coefficient robust against the outliers and indicates the correlation (not co-localization or overlap) between the two values. Manders coefficient quantitatively characterizes the level of overlap between the Voronoi polygons in two channels.

The aim of our study was to reveal for the first time the spatial organization of nuclear PIPs within individual nuclear sub-compartments and to quantitatively characterize the spatial relationship of the immunolabeled nuclear PI(4,5)P2, PI(3,4)P2 and PI(4)P with the nuclear speckle marker SON, with RNAPII and with nucleolar Fib. We quantitatively compare various analytical approaches and discuss their outcomes for the respective PIPs, within and between individual nuclear sub-compartments.

2. Material and methods

2.1. Cell culture

U-2 OS cells were grown in DMEM with 10% FBS at 37 °C and 5% CO_2. Cells were plated one day before staining in ~50% confluence on the high-precision 12 mm round coverslips treated with Hellmanex, sonicated, washed, dried and sterilized. U-2 OS cells stably expressing fibrillarin with SNAP-tag (Fib-SNAP) were described earlier [8].

2.2. Indirect immunofluorescence labeling

The cells were washed twice with PBS (pH 7.4) and fixed for 30 min in 2% PFA in PBS, washed 3-times for 5 min with PBS, then permeabilized in 0.1% Triton X-100 in PBS for 20 min, washed 3-times for 5 min by PBS and blocked in filtered 5% BSA in PBS for 30 min. Cells were incubated for 45 min with primary antibodies diluted in 5% BSA in PBS, washed 3-times for 5 min in PBS and incubated for 30 min with secondary antibodies diluted in 5% BSA in PBS. Then the cells were washed 3-times for 5 min in PBS, post-fixed for 15 min in 2% PFA in PBS and washed 3-times for 5 min in PBS. All procedures were performed at RT and the cells were stored in PBS.

2.3. Antibodies

Following primary antibodies and concentrations were used: mouse ascites IgM anti-PI(4,5)P2 2C11 (Z-A045; Echelon Biosci. Inc., USA) 5 μg/mL; mouse monoclonal IgG2 anti-PI(3,4)P2 (Z-P034; Echelon Biosci. Inc., USA) 5 μg/mL; mouse ascites IgM anti-PI(4)P (Z-P004; Echelon Biosci. Inc., USA) 5 μg/mL; rabbit polyclonal IgG anti-SON (ab121759; Abcam, UK) 1 μg/mL; rabbit polyclonal IgG anti-RNAPII CTD (ab210527; Abcam, UK) 3 μg/mL. Following secondary antibodies and concentrations were used: goat anti-mouse IgM (μ-chain) AF555 (A24126; Jackson ImmunoRes., UK) 10 μg/mL; goat anti-rabbit IgG AF647 (A21245; Invitrogen) 10 μg/mL.

2.4. SNAP labeling

Living U-2 OS cells stably expressing Fib-SNAP were incubated with 500 nM SNAP-Cell® SiR-647 (S9102S; New England BioLabs Inc., USA) in FluoroBrite DMEM (ThermoFisher) without serum for 45 min, washed 3-times with PBS, incubated for 45 min in FluoroBrite DMEM and washed 3-times with PBS before fixation and immunofluorescence labeling as described above.

2.5. dSTORM

Coverslips with cells were mounted in the Chamlide chamber (Live Cell Instrument, Korea) and covered with imaging buffer (PBS pH 7.4, 50 mM MEA). Single-molecule localizations (SMLs) data were acquired by Zeiss Elyra PS.1 equipped with HR Diode 642-150 and HR DPSS 561-200 lasers, Alpha Plan-Apochromat 100×/1.46 oil DIC M27 Elyra objective and Andor EM CCD iXon DU 897 camera and ZEN Black 2.1 SP3 software (Zeiss). AF647 and AF555 photo-switching was achieved by HiLo illumination and TIRF HP FOV with 100% power of 642 nm or 561 nm laser, and the signal was acquired via MBS 642 + EF LP 655 and MBS 561 + EF BP 570-620/LP 750 filters, respectively. Exposure time was 40 ms and EM gain was 300 for both channels.

2.6. Single-molecule localizations

SMLs were calculated in 2D by ZEN Black 2.1 SP3 software (Zeiss) using x,y 2D Gauss fit with point spread function (PSF) half width 177.9 nm, peak mask size 9 pixels and peak intensity to noise 6 and accounted for overlap in 2D with max cluster size 10. SMLs were rendered in ZEN software with 10 nm/px resolution and 1× PSF expansion factor. The data were model-based drift corrected in ZEN. Two channels were aligned with the affine fit and localization coordinates were exported as text files. Text files were converted into csv files and imported using self-written macro into the ImageJ2 [60] plug-in ThunderSTORM and visualized by normalized Gaussian method [61]. Random rotated localizations and images were created by swapping x and y coordinates [56]. Localization precision was measured by ZEN software.

2.7. Generator of simulated data

Randomly distributed SMLs were generated using ThunderSTORM ImageJ2 plug-in with respect to the number of frames, areas and molecular densities of the real data. Other parameters of the simulator were kept default.

2.8. Nearest neighbor analysis

Nearest neighbor distances (NNDs) were calculated in ThunderSTORM using self-written macro, radius step 50 nm and step count 10. Results were imported into Excel, normalized by the number of localizations in each acquisition and displayed as the normalized distributions of NNDs with error bars representing SEM. Mode (peak) NNDs and the fraction of the NNDs at the mode NND were calculated from the distributions in Excel (Microsoft). The data were statistically evaluated and the Tukey whisker graphs were created in Prism (GraphPad).

2.9. Voronoi tessellation

Localization data were imported in Coloc-Tesseler [59] as csv files and Spearman and Manders coefficients were calculated. Results were statistically evaluated and the Tukey whisker graphs were prepared in Prism (GraphPad).

2.10. Cross-correlation analysis

Tiff images were rendered from SMLM data using ThunderSTORM and analyzed by MatLab (MathWorks) R2019a function xcorr2. The results were normalized between 0 and 1 and displayed as color-coded intensities.

2.11. Statistics

Statistical comparison was done in Prism (GraphPad) using paired, one-tailed (NND analyses) or two-tailed (CT analyses) *t*-test for the normally distributed data tested by Kolmogorov-Smirnov test. Statistical significance was expressed as follows: *P < 0.05; **P < 0.01; ***P < 0.005.

3. Results

3.1. Nanoscale visualization of nuclear PI(4,5)P2

We used dSTORM to resolve with nanometer precision the spatial organization of nuclear PI(4,5)P2. First we immunolabeled nuclear PI(4,5)P2 with the primary antibody 2C11 and two secondary antibodies conjugated with Alexa Fluor (AF) 555 and AF647 (PI(4,5)P2-AF555 and PI(4,5)P2-AF647, resp.) (Fig. 1A–C). The specificity of anti-PI(4,5)P2 antibody 2C11 was previously validated and it reliably detects nuclear PI(4,5)P2 [15,20,22,24]. We used two different secondary antibodies against one primary antibody to experimentally find the ideal degree of the co-patterning between the two channels. We compared the real data either with the single-molecule localizations (SMLs) randomized by rotation (rand. rotated) according to Dunn et al. [56] (Fig. 1D) or with the SMLs randomly generated (rand. generated) (Fig. 1E) by ThunderSTORM [61] plug-in of ImageJ2 [60]. This allowed us to assess by two independent methods if the co-patterning of the two probes is non-random. We localized PI(4,5)P2-AF555 and PI(4,5)P2-AF647 with the precision 18.6 ± 1 nm and 22.4 ± 0.7 nm, resp., and from the SML data, we first calculated using ThunderSTORM the NNDs between PI(4,5)P2-AF555 and PI(4,5)P2-AF647. Then, we normalized the number of localizations at individual NND bins by the total number of localizations and plotted the results as the normalized distributions of NND (Fig. 1F). From the normalized NND distributions we calculated the mode (most frequent) NND and the fraction of the NND at mode NND. The mode of the real NND was 6.3 ± 0.5 nm, which was increased ~40% ($P < 0.005$; $N = 6$) for rand. rotated SMLs to 8.8 ± 0.9 nm and ~120% increased ($P < 0.005$; $N = 6$) to 14 ± 1.7 nm for rand. generated SMLs (Fig. 1G). The fraction of the real NND at the mode NND was 5.8 ± 0.6%, which was ~43% decreased ($P < 0.005$; $N = 6$) for rand. rotated SMLs and ~19% decreased ($P < 0.005$; $N = 6$) for rand. generated SMLs (Fig. 1H). For the *in-cellulo* visualization of the spatial organization of nuclear PIPs, we developed a visualization tool that enables color-coding of the pixels according to the pair-wise NND of the SMLs in one channel with the respect to SMLs in the second channel. Fig. 1I shows the *in-cellulo* map in which the pixels are color-coded according to NND of the PI(4,5)P2-AF555 to PI(4,5)P2-AF647 in the real image. In contrast, Fig. 1J and K illustrate the increased NND in the rand. rotated and rand. generated images, resp.

In addition to the NND analysis, we evaluated the co-patterning of PI(4,5)P2-AF555 with PI(4,5)P2-AF647 by Spearman rank correlation and Manders overlap coefficients calculated by CT [59]. Spearman and Manders coefficients characterize the level of correlation and overlap, resp., on the scale from −1 (anti-correlation or inverse overlap) through 0 (no correlation or no overlap) to 1 (maximal correlation or maximal overlap) between the Voronoi polygons in two channels. Spearman correlation coefficient of the real data was 0.57 ± 0.03 and it was reduced ~8-fold ($P < 0.001$; $N = 6$) for rand. rotated to 0.07 ± 0.02 and more than 70-fold ($P < 0.001$; $N = 6$) for rand. generated to −0.008 ± 0.006 (Fig. 1L). Manders overlap coefficient of the real data was 0.54 ± 0.06 and it was reduced ~2.5-fold ($P < 0.005$; $N = 6$) for rand. rotated to 0.15 ± 0.02 and ~11-fold ($P < 0.005$; $N = 6$) for rand. generated to 0.05 ± 0.01 (Fig. 1M). Spearman and Manders coefficients were affected by

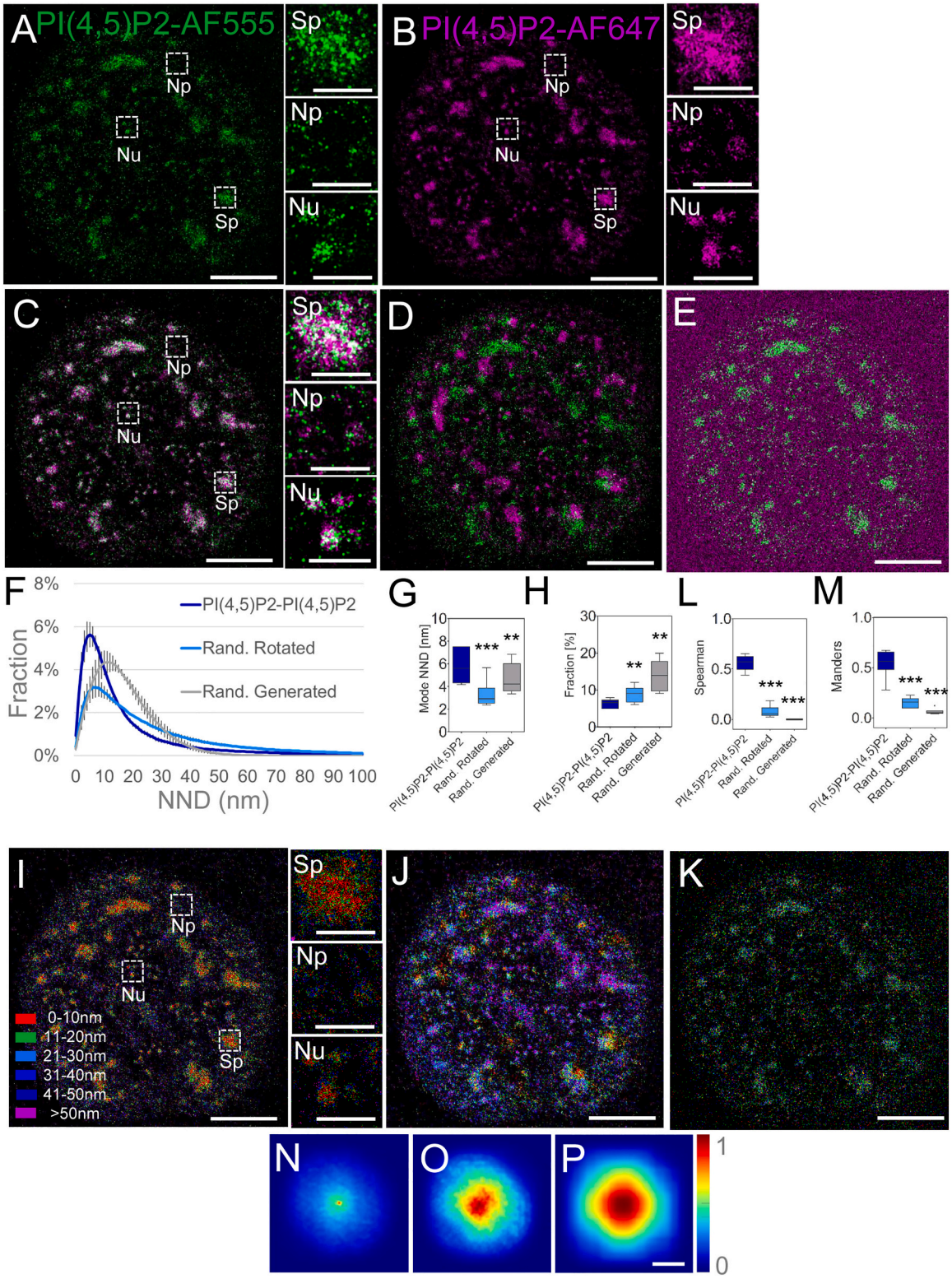

Fig. 1. dSTORM imaging and distribution analysis of the nuclear PI(4,5)P2. Nuclear PI(4,5)P2 indirectly immunolabeled with AF555 (A) and AF647 (B), imaged by dSTORM and visualized as normalized Gaussian fit of the point spread function into the individual localizations; merged image (C) and zoom-in to the boxed regions of a nuclear speckle (Sp), nucleoplasm (Np) and nucleolus (Nu). Merged image of PI(4,5)P2-AF555 and PI(4,5)P2-AF647 randomized by rotation (D) or by generating randomly distributed PI(4,5)P2-AF647 signal (E). (F) Normalized distribution of the NND between PI(4,5)P2-AF555 and real (PI(4,5)P2-PI(4,5)P2), randomized by rotation (Rand. Rotated) or randomly generated (Rand. Generated) PI(4,5)P2–AF647 localizations. The most frequent (Mode) NND (G) and their fraction (H), Spearman rank correlation (L) and Manders overlap (M) coefficients between PI(4,5)P2-PI(4,5)P2, Rand. Rotated and Rand. Generated data. Color-coded pixel maps of the real (I), Rand. Rotated (J) and Rand. Generated (K) PI(4,5)P2-AF555 to PI(4,5)P2-AF647 NNDs with the legend for I–K in I. Cross-correlation (CC) intensities of the real (N) Rand. Rotated (O) and Rand. Generated (P) PI(4,5)P2-AF555 and PI(4,5)P2–AF647. The calibration bar shows the relative level of CC. Scale bars = 5 μm; 1 μm in zoom-in images and 50 nm in the CC.

the randomization to a greater extent than the mode NND or the fraction of the NND at mode NND. Rand. generated data displayed a much greater reduction of Spearman and Manders coefficients than the rand. rotated data compared to the real data.

A cross-correlation (CC) is a measure of similarity of two series as a function of the displacement of one series relative to the other. It enables to find the regions in which two images most resemble each other. We performed CC analysis of the representative real (Fig. 1N), rand. rotated (Fig. 1O) and rand. generated (Fig. 1P) images and displayed the results as the spatial distribution maps showing the color-coded degrees of CC between PI(4,5)P2-AF555 and PI(4,5)P2-AF647 on the normalized, color-coded scale from 0 (no CC) to 1 (highest CC). Sharply centered high CC intensities of the real representative image (Fig. 1N) indicate strong CC between PI(4,5)P2-AF555 and PI(4,5)P2-AF647. Scattered CC intensities of the representative rand. rotated (Fig. 1O) and rand. generated (Fig. 1P) images indicate the loss of CC between PI(4,5)P2-AF555 and randomized PI(4,5)P2-AF647.

Taken together, we optimized the dual-color dSTORM image acquisition, generation of the randomized SMLs and quantitative comparison of the real and randomized data using several parameters and independent methods. Next, we used this pipeline to characterize the spatial relationship of PI(4,5)P2 with the nuclear speckle marker SON, with RNAPII, and with Fib in the nucleoli. Furthermore, we have also applied this analytical pipeline to study other nuclear PIPs, namely PI(3,4)P2 and PI(4)P.

3.2. PI(4,5)P2 concentrates in the nuclear speckles

Localization of PI(4,5)P2 to the nuclear speckles has been previously reported [15,20,22], but the precise analysis of the PI(4,5)P2 distribution within nuclear speckles is missing. Therefore, we performed dual-color dSTORM imaging of PI(4,5)P2-AF555 and the nuclear speckle marker SON immunolabeled with AF647 (SON-AF647) (Fig. 2A–C). We localized PI(4,5)P2-AF555 and SON-AF647 with the precision 20.2 ± 0.8 nm and 24.5 ± 1.6 nm, resp. SON-AF647 visualized by dSTORM displayed a matrix-like pattern (Fig. 2B) with PI(4,5)P2-AF555 dispersed within the SON matrix (Fig. 2A–C, arrowheads). We calculated the global (throughout the whole nucleus) NND between PI(4,5)P2-AF555 and SON-AF647 SMLs for the real (Fig. 2C), rand. rotated (Suppl. Fig. 1A) and rand. generated (Suppl. Fig. 1B) SMLs. From the normalized NND distributions (Fig. 2D) we calculated the global mode NND of 6.7 ± 0.6 nm, which was increased ~100% ($P < 0.005$; $N = 6$) for the rand. rotated to 13.5 ± 2 nm and ~240% ($P < 0.005$; $N = 6$) for the rand. generated to 22.8 ± 2.9 nm (Fig. 2E). The fraction of NND at the mode NND was 2.9 ± 0.2% and this was ~38% decreased ($P < 0.005$; $N = 6$) for rand. rotated SMLs to 1.8 ± 0.2% but unaffected for rand. generated SMLs where it was 2.9 ± 0.3% (Fig. 2F). Rand. rotated SON-AF647 retained clustered pattern, but SON-AF647 clusters were moved away from the nuclear speckle associate PI(4,5)P2 and therefore the fraction of the NND at the mode NND is significantly different from the real data. In contrast, rand. generated SON-AF647 does not display clustered patterns but localizes to the proximity of the nuclear speckle associate PI(4,5)P2 and therefore the fraction of the rand. rotated NND at the mode NND was not significantly different from the real data. The color-coded pixel map of the NND of PI(4,5)P2-AF555 to SON-AF647 shows the close proximity of PI(4,5)P2 to SON in nuclear speckles (Fig. 2G) and this spatial relationship was disrupted in the case of rand. rotated (Suppl. Fig. 1C) and rand. generated (Suppl. Fig. 1D). These data on the global NND of PI(4,5)P2 to SON show that their co-distribution is non-random. However, contrary to SON, which localizes only to nuclear speckles, PI(4,5)P2 localizes to the nuclear speckles and also to the nucleoplasm and nucleoli. Therefore, we analyzed 1.5 × 1.5 μm regions of interest (ROIs) around nuclear speckles and characterized the local NND of PI(4,5)P2 to SON. The local mode NND of PI(4,5)P2-AF555 to SON-AF647 was 4 ± 0.2 nm. It was not significantly affected for rand. rotated SMLs, where it was 3.8 ± 0.1 nm, but it was increased ~40% ($P < 0.005$; $N = 12$) for rand. generated SMLs to 5.7 ± 0.2 nm. Rand. rotated ROIs retain their clustered SON-AF647 pattern that overlaps with PI(4,5)P2-AF555 and therefore their mode NND does not significantly differ from the real NND. In contrast, rand. generated ROIs did not display clustered SON-AF647 pattern, which led to the significantly increased mode NND compared to the real NND. Fraction of the local NND at the mode NND for the real SMLs was 12.6 ± 0.5% and it was ~7% ($P < 0.05$; $N = 12$) decreased for rand. rotated SMLs to 11.7 ± 0.6% but unaffected for rand. generated SMLs, where it was 12.3 ± 0.4%. Comparison between the global and local analysis shows that the global analysis is biased by PI(4,5)P2 which does not localize to the nuclear speckles but to the nucleoplasm and nucleoli and therefore is at the greater distances to SON than the nuclear speckle-localized PI(4,5)P2.

The global correlation of PI(4,5)P2-AF555 with SON-AF647 was characterized by Spearman coefficient 0.59 ± 0.03, which was more than a magnitude reduced ($P < 0.005$; $N = 6$) in the case of rand. rotated SMLs to 0.05 ± 0.04 and in the case of rand. generated to −0.005 ± 0.007 (Fig. 2H). The overlap of Voronoi polygons surrounding PI(4,5)P2-AF555 and SON-AF647 SMLs was characterized by Manders coefficient 0.65 ± 0.05, which was 6.5-fold reduced ($P < 0.005$; $N = 6$) for rand. rotated SMLs to 0.1 ± 0.02 and more than 20-fold reduced ($P < 0.005$; $N = 6$) in the case of rand. generated SMLs to 0.03 ± 0.004 (Fig. 2I). The local correlation of PI(4,5)P2-AF555 with SON-AF647 in the 1.5 × 1.5 μm ROIs around speckles was characterized by Spearman coefficient 0.39 ± 0.03, which was reduced 1.5-fold ($P < 0.01$; $N = 10$) in the case of rand. rotated SMLs to 0.25 ± 0.03 and 78-fold reduced ($P < 0.005$; $N = 10$) to 0.005 ± 0.03 in the case of rand. generated SMLs (Fig. 2H). The local overlap of Voronoi polygons surrounding PI(4,5)P2-AF555 and SON-AF647 localizations was characterized by Manders coefficient 0.27 ± 0.02, which was 1.3-fold reduced ($P < 0.05$; $N = 10$) in the case of rand. rotated SMLs to 0.21 ± 0.02 and 2.7-fold reduced ($P < 0.005$; $N = 10$) in the case of rand. generated SMLs (Fig. 2I).

Finally, we analyzed by CC the representative real (Fig. 2J) rand. rotated (Fig. 2K) and rand. generated (Fig. 2L) images and displayed the results as the spatial distribution maps showing the color-coded CC between PI(4,5)P2-AF555 and SON-AF647. Sharply centered CC intensities of the real representative image (Fig. 2J) indicate the strong CC between PI(4,5)P2-AF555 and SON-AF647. Scattered CC intensities of the representative rand. rotated image (Fig. 2K), and even more in the case of rand. generated image (Fig. 2L), indicates reduced CC between PI(4,5)P2-AF555 and randomly distributed SON-AF647.

3.3. A subset of nuclear PI(4,5)P2 foci localize to the close proximity of RNAPII

Previous research suggests that nucleoplasmic PI(4,5)P2 forms 40–100 nm foci where the RNAPII transcription machinery concentrates [22]. Therefore, we investigated in detail the spatial relationship between PI(4,5)P2-AF555 and RNAPII immunolabeled with AF647 (RNAPII-AF647) by dual-color dSTORM. We localized PI(4,5)P2-AF555 and RNAPII-AF647 with the precision 19.3 ± 0.8 nm and 24 ± 0.6 nm, resp., and found that RNAPII localizes in addition to small nucleoplasmic foci also to the periphery of nuclear speckles (Fig. 3A–C). Therefore, we separately evaluated the global NND between PI(4,5)P2-AF555 and RNAPII-AF647 (Fig. 3D) and their local NND within 1.5 × 1.5 μm ROIs in the nucleoplasm and around nuclear speckles. However, the global NND differed neither from that measured in the ROIs of nucleoplasm nor nuclear speckles (Suppl. Fig. 2A). The mode global NND 5.6 ± 0.3 nm was ~7% increased ($P < 0.05$; $N = 7$) to 6 ± 0.4 nm for the rand. rotated SMLs (Fig. 3E; Suppl. Fig. 2B) and ~54% increased ($P < 0.005$; $N = 7$) to 8.6 ± 0.5 nm for the rand. generated SMLs (Fig. 3E; Suppl. Fig. 2D). The fraction of the global NND at the mode NND of the real data was 7.6 ± 0.6% and it was ~46% reduced ($P < 0.01$; $N = 7$) for rand. rotated SMLs to 4.1 ± 0.3% and not significantly changed for rand. generated SMLs ($N = 7$), where it was 7.4 ± 0.4% (Fig. 3F). The color-

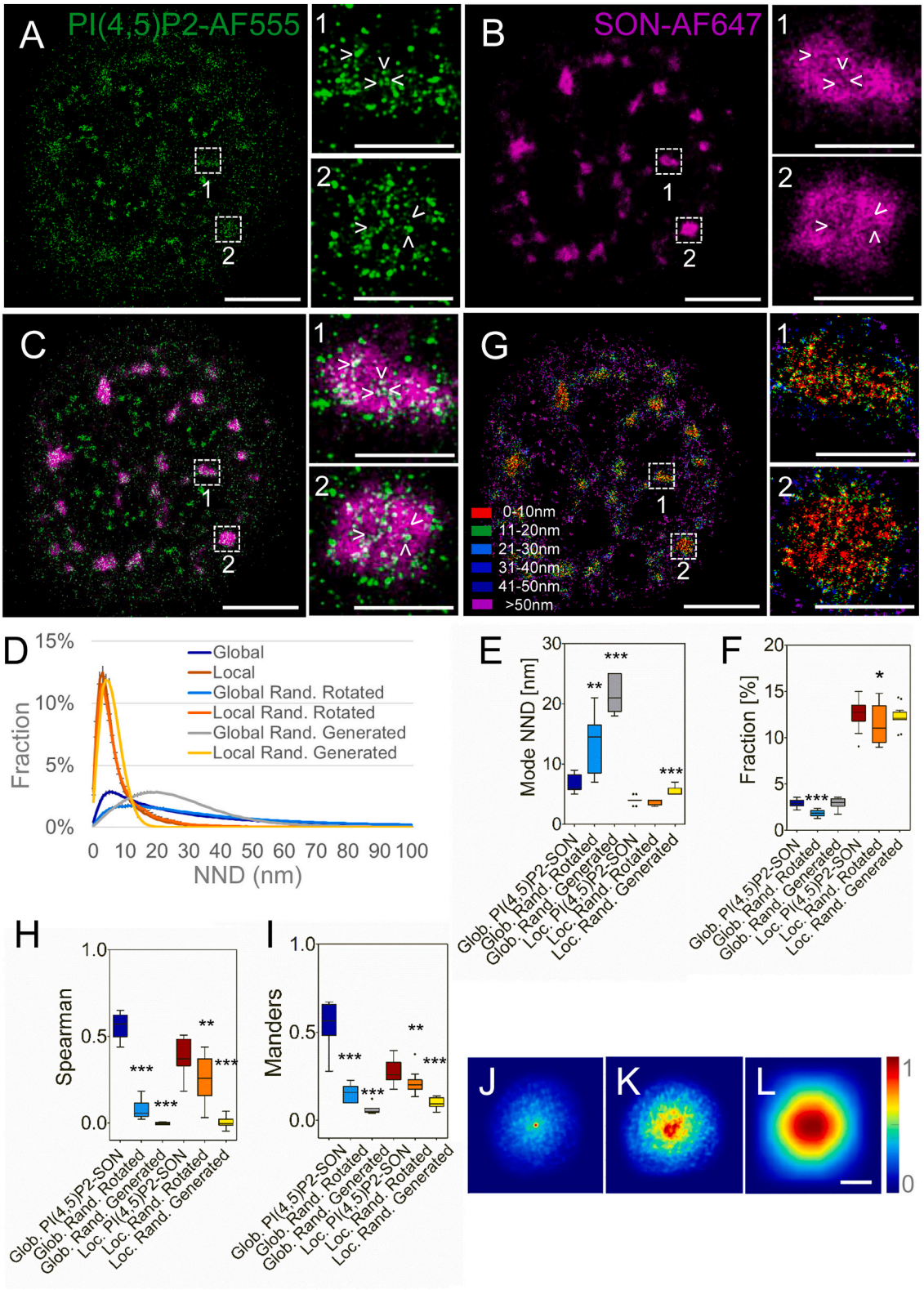

Fig. 2. dSTORM imaging and distribution analysis of PI(4,5)P2 with respect to the nuclear speckle marker SON. PI(4,5)P2 immunolabeled with AF555 (A) and SON-AF647 (B) imaged by dSTORM and visualized as normalized Gaussian fit of the point spread function into the individual localizations, merged image (C) and zoom-in to the boxed nuclear speckles. (D) Normalized distribution of the Global (Glob.) and Local (Loc.) NND between PI(4,5)P2-AF555 and SON-AF647 in the real (PI(4,5)P2-SON), randomized by rotation (Rand. Rotated) or randomly generated (Rand. Generated) images. (E) Color-coded pixel map of the NND of PI(4,5)P2-AF555 to SON-AF647 with zoom-in to the boxed speckles. The mode NNDs (F) and their fraction (G), Spearman rank correlation (H) and Manders overlap (I) coefficients between PI(4,5)P2 and SON, Rand. Rotated and Rand. Generated Glob. and Loc. data. Cross-correlation (CC) intensities of the real (J) Rand. Rotated (K) and Rand. Generated (L) PI(4,5)P2-AF555 and SON–AF647. Scale bars = 5 μm; 1 μm in the zoom-in images and 50 nm in the CC visualization. The calibration bar shows the relative CC level.

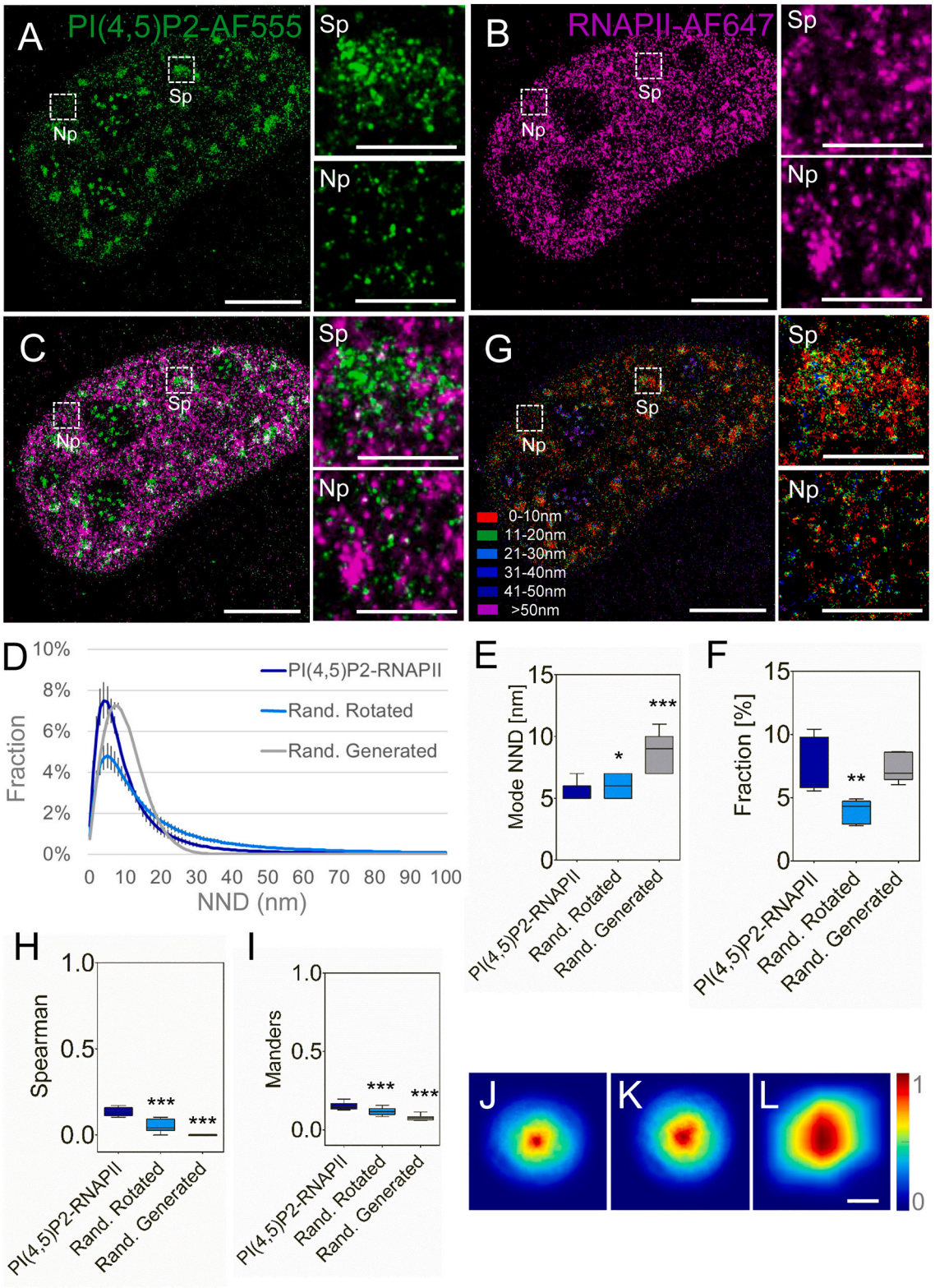

Fig. 3. dSTORM imaging and distribution analysis of the spatial relationship between PI(4,5)P2 and RNAPII. PI(4,5)P2 indirectly immunolabeled with AF555 (A) and RNAPII-AF555 (B) imaged by dSTORM and visualized as normalized Gaussian fit of the point spread function into the individual localizations, merged image (C) and zoom-in to the boxed regions of a nuclear speckle (Sp) and nucleoplasm (Np). (D) Normalized distribution of the NND between PI(4,5)P2-AF555 and RNAPII-AF647 in the real (PI(4,5)P2-RNAPII), randomized by rotation (Rand. Rotated) or randomly generated (Rand. Generated) images. The most frequent (Mode) NND (E) and their fraction (F). (G) Color-coded pixel map of the NND of PIP2-AF555 to RNAPII-AF647 with zoom-in to the boxed Sp and Np regions. Spearman rank correlation (H) and Manders overlap (I) coefficients between PI(4,5)P2 and RNAPII, Rand. Rotated and Rand Generated data. Cross-correlation (CC) intensities of the real (J) Rand. Rotated (K) and Rand. Generated (L) PI(4,5)P2-AF555 and RNAPII–AF647. Scale bars = 5 μm; 1 μm in the zoom-in images and 50 nm in the CC visualization. The calibration bar shows the relative CC level.

coded pixel map of the NND of PI(4,5)P2-AF555 to RNAPII-AF647 shows the close proximity of a subset of PI(4,5)P2 foci to RNAPII in the nucleoplasm and nuclear speckles (Fig. 3G), which was disturbed in the case of rand. rotated (Suppl. Fig. 2D) and rand. generated (Suppl. Fig. 2E) RNAPII-AF647 SML data.

Taken together, the global distribution of PI(4,5)P2 in respect to RNAPII is non-random. The global NND analysis of the spatial relationship between PI(4,5)P2 and RNAPII, which localizes to the nucleoplasm and nuclear speckles, is not biased by the contribution of the remaining minor fraction of nucleolar PI(4,5)P2. This is in contrast to the spatial relationship between PI(4,5)P2 and the nuclear speckle marker SON, where the global NND analysis was biased by the relatively larger contribution of the nucleoplasmic PI(4,5)P2. Randomization by rotation affected the mode NND less than randomization by generating random SMLs. This could be explained by clustering of RNAPII in small foci in the real and rand. rotated data and by the fact that those foci are absent in the rand. generated images. On the other hand randomization by rotation, but not randomly generated SMLs, significantly affected the fraction of NND at the mode NND. This further supports the notion of clustering of RNAPII in small foci in the real and rand. rotated data, contrary to the rand. generated data. A higher fraction of individual rand. generated SMLs localize to the proximity of PI(4,5)P2 foci, but in the case of rand. rotated RNAPII-AF647, SMLs retain their clustered pattern and by rotation of images those clusters are separated from their originally proximal PI(4,5)P2-AF555 foci.

Furthermore, we characterized the correlation and overlap between PI(4,5)P2-AF555 and RNAPII-AF647 by Spearman and Manders coefficients, resp. The correlation of PI(4,5)P2-AF555 with RNAPII-AF647 was characterized by Spearman coefficient 0.13 ± 0.01, which was ~2.5-fold ($P < 0.005$; $N = 7$) reduced for rand. rotated to 0.05 ± 0.01 and diminished to 0 ($P < 0.005$; $N = 7$) for rand. generated SMLs (Fig. 3H). The overlap of PI(4,5)P2-AF555 with RNAPII-AF647 was characterized by Manders coefficient 0.15 ± 0.01, which was ~20% reduced ($P < 0.01$; $N = 7$) to 0.12 ± 0.01 for rand. rotated and ~2-fold reduced ($P < 0.005$; $N = 7$) to 0.07 ± 0.01 for rand generated (Fig. 3I). Taken together, the correlation and overlap analyses showed the non-random co-distribution of PI(4,5)P2-AF555 with RNAPII-AF647, which is in agreement with our NND analyses. However, by the correlation and overlap analyses the co-distribution of PI(4,5)P2 with RNAPII is lower than the co-distribution of PI(4,5)P2 with SON. This is due to the fact that PI(4,5)P2-AF555 and RNAPII-AF647 form small foci that do not largely overlap due to their small size resolved by dSTORM, but tend to localize in the close proximity, which is documented by the mode NND 5.6 ± 0.3 nm (Fig. 3F) between PI(4,5)P2-AF55 and RNAPII-AF647.

Finally, we performed CC analysis of the representative real (Fig. 3J), rand. rotated (Fig. 3K) and rand. generated (Fig. 3L) images and displayed the results as the color-coded CC maps between PI(4,5)P2-AF555 and RNAPII-AF647. Slightly scattered CC intensities of the real representative image (Fig. 3J) reflected the lower Spearman correlation and lower Manders overlap of PI(4,5)P2-AF555 with RNAPII-AF647 compared to PI(4,5)P2-AF555 with PI(4,5)P2-AF647 or PI(4,5)P2-AF555 with SON-AF647. CC intensities appear more scattered for the rand. rotated (Fig. 3K) and even more rand. generated then those of the real representative image. This reflects the lower (as compared to PI(4,5)P2-AF555 with PI(4,5)P2-AF647 or PI(4,5)P2-AF555 with SON-AF647) but non-random co-distribution of PI(4,5)P2-AF555 with RNAPII-AF647. Taken together, we showed with nanometer precision that a subset of nucleoplasmic PI(4,5)P2-AF555 foci localize to the close proximity of RNAPII-AF647 clusters and that RNAPII-AF647 also clusters within or around nuclear speckles.

3.4. Nucleolar PI(4,5)P2 is surrounded by fibrillarin

Fib was previously shown by SIM to form in the nucleoli the donut-shaped patterns in which the center is filled with PI(4,5)P2 [8]. Here we used Fib fused to the self-labeling SNAP tag (Fib-SNAP) and stably exogenously over-expressed in the U-2 OS cell line due to the lack of reliable primary antibodies for the immunofluorescence detection of endogenous Fib [8]. We localized PI(4,5)P2-AF555 and Fib-SNAP-SiR647 with the precision 19.3 ± 3 nm and 25.7 ± 2.7 nm, resp., and found that the nucleolar PI(4,5)P2-AF555 is almost radially surrounded by the regularly patterned Fib-SNAP-SiR647 (Fig. 4A–C). We quantitatively evaluated the global and local spatial relationship of PI(4,5)P2-AF555 with Fib-SNAP-SiR647 throughout the whole nucleus and in the 2x2μm ROIs around the Fib-SNAP-SiR647, resp. The distribution of the global NND between PI(4,5)P2-AF555 and Fib-SNAP-SiR647 starkly differed from the local NND (Fig. 4D) because PI(4,5)P2-AF555 distributes predominantly to the nuclear speckles and nucleoplasm and nucleolar PI(4,5)P2 represents only a minor subpopulation, while Fib-SNAP-SiR647 is almost exclusively localized in the nucleoli. This situation was illustrated by the color-coded pixel map of the NND of PI(4,5)P2-AF555 to Fib-SNAP-SiR647 (Fig. 4E; Suppl Fig. 3C, D), in which the pixels corresponding to the NND of PI(4,5)P2-AF555 to Fib-SNAP-SiR647 < 50 nm are almost exclusively localized to the nucleoli. The specific localization of Fib to the nucleoli, in contrast to the broad distribution of PI(4,5)P2 with only its minor fraction localized in the nucleoli, are also documented by the mode global NND 14.4 ± 1.3 nm. The mode global NND is almost 2-fold higher than the mode local NND 7.5 ± 0.4 nm (Fig. 4F). Global increase ~47% ($P < 0.05$; $N = 5$) to 21.2 ± 4.8 nm for the rand. rotated and ($P < 0.05$; $N = 5$) ~3-fold to 44.6 ± 12.7 nm for the rand. generated SMLs (Suppl. Fig. 3A, B) showed that the spatial relationship between PI(4,5)P2 and Fib-SNAP-SiR647 is non-random. The fraction of the global NND at the mode NND was 1.6 ± 0.3% and it was ~4-fold reduced for the rand. rotated SMLs ($P < 0.05$; $N = 5$) to 0.4 ± 0.1% but not significantly affected for the rand. generated SMLs where it was 2.1 ± 0.8%. However, it is important to note that the fraction of the global NND at the mode NND of the real and rand. generated SMLs were derived from the mode NNDs that differed 3-fold. The local mode NND of the real PI(4,5)P2-AF555 to Fib-SNAP-SiR647 7.5 ± 0.4 nm was ~20% increased ($P < 0.05$; $N = 10$) to 9 ± 0.5 nm for the rand. rotated and ~60% increased ($P < 0.05$; $N = 10$) to 12.1 ± 2.1 nm for the rand. generated SMLs (Fig. 4F; Suppl. Fig. 3E–G). The fraction of the local NND at the mode NND of the real SMLs 5.7 ± 0.5% neither differed significantly from the rand. rotated (5.4 ± 0.7%) nor from rand. generated SMLs (5.3 ± 0.4%) (Fig. 4G). This shows that the molecule densities in the ROIs do not differ between real and randomized images but the close proximity of Fib-SNAP-SiR647 specifically arranged around PI(4,5)P2-AF555 nucleolar foci is disrupted by both randomization methods.

Spearman and Manders coefficients of the real, rand. rotated and rand. generated SMLs of PI(4,5)P2-AF555 and Fib-SNAP-SiR647 (Fig. 4H and I) supported our conclusions from the distance analyses. The global Spearman correlation and Manders overlap coefficients of PI(4,5)P2-AF555 with Fib-SNAP-SiR647 were slightly but significantly reduced ($P < 0.05$; $N = 5$) by the randomization (Suppl. Tables 1, 2). Neither the local Spearman correlation coefficient nor Manders overlap coefficient of PI(4,5)P2-AF555 with Fib-SNAP-SiR647 were significantly affected for rand. rotated. However, the local Spearman and Manders coefficients were significantly reduced ($P < 0.01$ and $P < 0.005$ resp.; $N = 10$) for rand. generated SMLs (Fig. 4H and I). The randomization by rotation had a small or no effect on NND analyses, Spearman and Manders coefficients due to the unique geometry of PI(4,5)P2 and Fib in the nucleoli, where Fib surrounds PI(4,5)P2 but does not largely overlap with it. Therefore, rotating Fib-SNAP-SiR647 SMLs around PI(4,5)P2-AF555 SMLs (compare Fig. 4C1, 2 with Suppl. Fig. 3E, F) results in their co-patterning very similar to that of the real SMLs and randomization by rotation of one channel in respect to the second channel is not suitable for the symmetrical patterns.

Finally, we analyzed by CC the representative global (Suppl. Fig. 3H–J) and local (2 × 2 μm ROI) real (Fig. 4J). rand. rotated (Fig. 4K) and rand. generated (Fig. 4L) images. Their comparison reflects the most

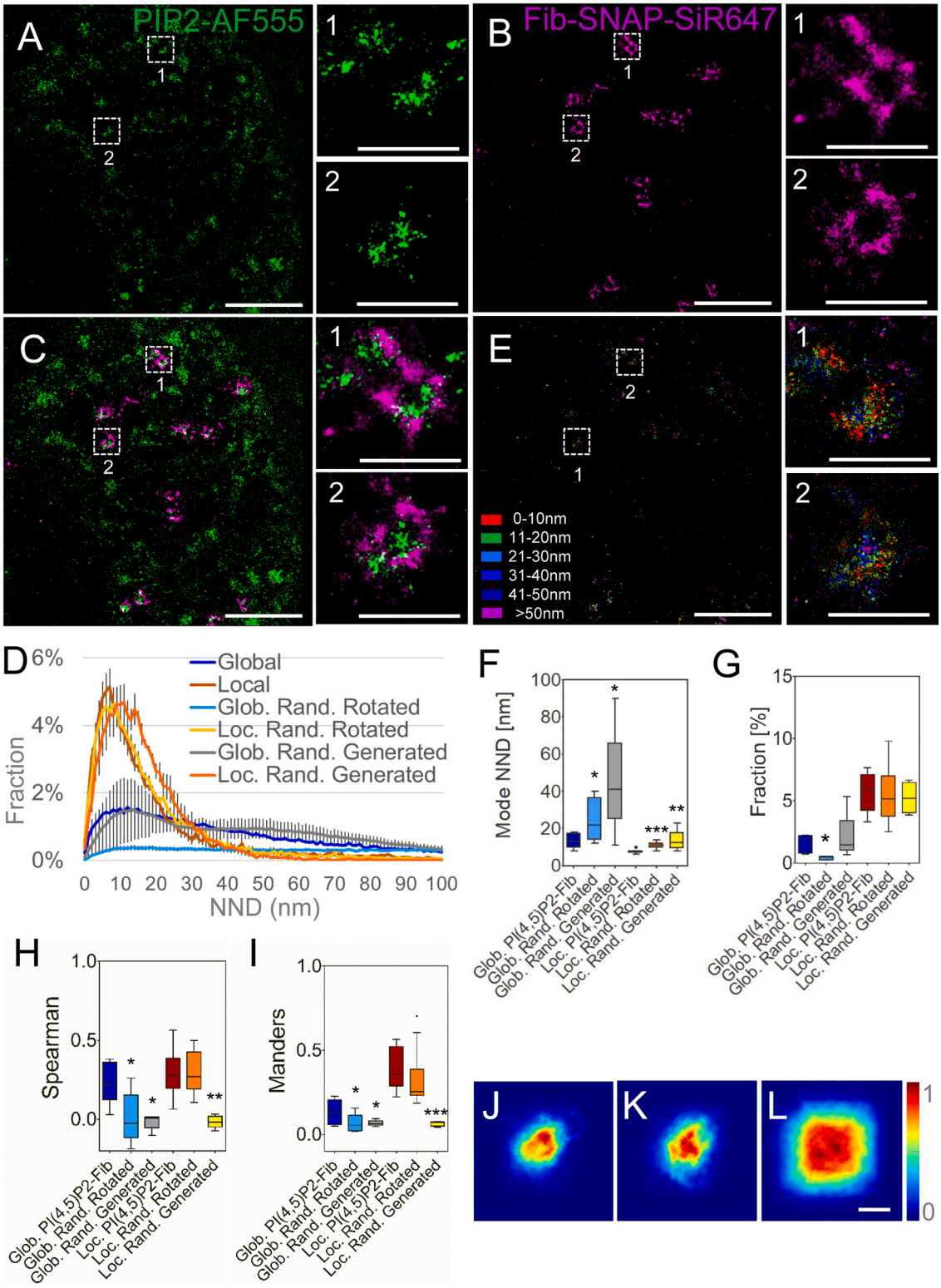

Fig. 4. dSTORM imaging and distribution analysis of the nucleolar PI(4,5)P2 and fibrillarin. A cell with indirectly immunolabeled PI(4,5)P2-AF555 (A) and stably expressing fibrillarin-SNAP (Fib-SNAP) labeled with Cell SNAP SiR-647 (Fib-SNAP-SiR647) (B) imaged by dSTORM and visualized as normalized Gaussian fit of the point spread function into the individual localizations, merged image (C) and zoom-in to the boxed nucleolar regions (1, 2). (D) Distribution of the Global and Local NND between PI(4,5)P2-AF555 and Fib-SNAP-SiR647 in the real (PI(4,5)P2-Fib-SNAP-SiR647), randomized by rotation (Rand. Rotated) or randomly generated (Rand. Generated) images. (E) Color-coded pixel map of the NND of PIP2-AF555 to Fib-SNAP-SiR647 with zoom-in to the boxed nucleoli (1, 2). The most frequent (Mode) NND (F) and their fraction (G), Spearman rank correlation (H) and Manders overlap (I) coefficients between PI(4,5)P2 and Fib-SNAP-SiR647, Rand. Rotated and Rand. Generated Global and Local data. Cross-correlation (CC) intensities of the real (J) Rand. Rotated (K) and Rand. Generated (L) PI(4,5)P2-AF555 and Fib-SNAP-SiR647. Scale bars = 5 μm; 1 μm in the zoom-in images and 50 nm in the CC visualization. The calibration bar shows the relative CC level.

disrupting effect of the rand. generated Fib-SNAP-SiR647 SMLs on the PI(4,5)P2-AF555 CC with Fib-SNAP-SiR647 and supports our conclusions from the NND, Spearman and Manders analyses. Specific and clearly non-random co-distribution of PI(4,5)P2 localized to the nucleolar FC radially surrounded by Fib localized to the nucleolar DFC is largely disrupted by random re-distribution of Fib-SNAP-SiR647 SMLs but not by rotating Fib-SNAP-SiR647 with respect to the PI(4,5)P2. Taken together, PI(4,5)P2 displays a unique spatial relationship with Fib that differs from the co-distribution of PI(4,5)P2 with the nuclear speckle marker SON or RNAPII.

3.5. Nuclear PI(3,4)P2 localizes to nuclear speckles and to the close proximity of RNAPII

Localization of PI(3,4)P2 in the cell nucleus has been previously reported [24,25]. However, the detailed information about its sub-nuclear localization and spatial relationship with nuclear markers is missing. Therefore, in order to broaden our understanding of the nuclear roles of PI(3,4)P2, we analyzed its spatial relationship with the nuclear speckle marker SON and with RNAPII. We observed by dSTORM the PI(3,4)P2 signal concentrated in sub-nuclear regions and scattered in the nucleoplasm (Fig. 5), which was reminiscent of PI(4,5)P2 (Figs. 1–3) with the exception of nucleoli. Dual-color dSTORM imaging of PI(3,4)P2-AF555 (Fig. 5A) and the nuclear speckle marker SON-AF647 (Fig. 5B) showed PI(3,4)P2-AF555 dispersed within the SON matrix (Fig. 5C), similarly to PI(4,5)P2 (Fig. 2C). We measure the NND between PI(3,4)P2-AF555 and SON-AF647 in the real, (Fig. 5D), rand. rotated (Suppl. Fig. 4A) rand. generated SMLs (Suppl. Fig. 4B). The color-coded pixel map calculated from the real NND of PI(3,4)P2-AF555 to SON-AF647 showed the close proximity of PI(3,4)P2 to SON in nuclear speckles (Fig. 5E). This proximity was diminished in the rand. rotated (Suppl. Fig. 4C) and rand. generated (Suppl. Fig. 4D) SMLs. From the NND distributions, we calculated the mode NND of 3.6 ± 0.3 nm, which was increased ~77% ($P < 0.005$; $N = 8$) for the rand. rotated and more than ~3-fold increased ($P < 0.05$; $N = 9$) for the rand. generated SMLs (Fig. 5F). The fraction of the NND at the mode NND of the real SMLs was 9.5 ± 1.1% and this was more than 2-fold reduced ($P < 0.005$; $N = 8$) for the rand. rotated and ~30% reduced ($P < 0.05$; $N = 8$) for the rand. generated SMLs (Fig. 5G).

The correlation of PI(3,4)P2-AF555 with SON-AF647 was characterized by Spearman coefficient 0.58 ± 0.04, which was ~8-fold reduced ($P < 0.005$; $N = 8$) in the case of rand. rotated SMLs to 0.07 ±

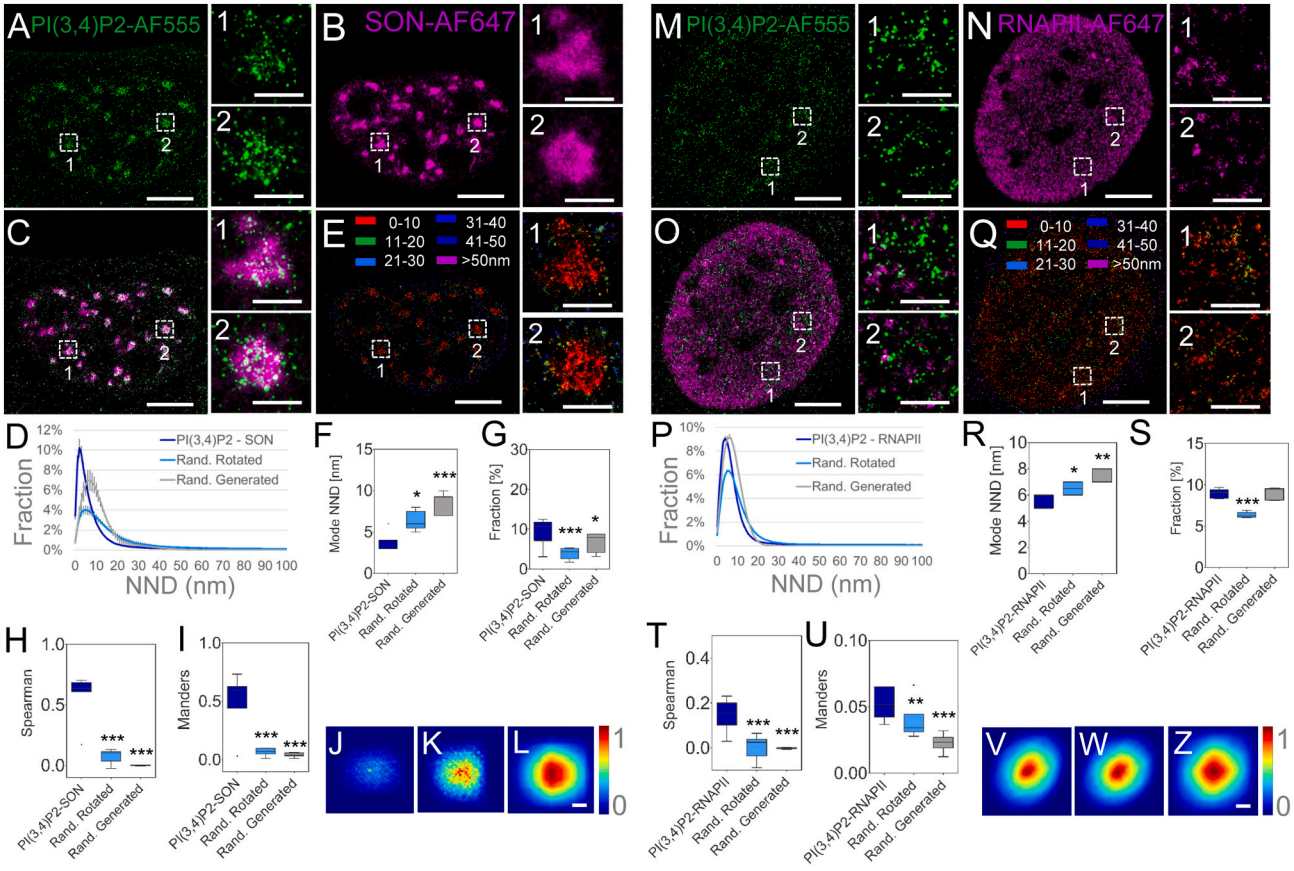

Fig. 5. dSTORM imaging and distribution analysis of PI(3,4)P2 with respect to the nuclear speckle marker SON and RNAPII. PI(3,4)P2-AF555 (A) and SON-AF647 (B) imaged by dSTORM and visualized as normalized Gaussian fit of the point spread function (PSF) into the individual localizations, merged image (C) and zoom-in to the boxed nuclear speckles (1, 2). (D) Distribution of the Global and Local NND between PI(3,4)P2-AF555 and SON-AF647 in the real (PI(3,4)P2-SON), randomized by rotation (Rand. Rotated) or randomly generated (Rand. Generated) images. (E) Color-coded pixel map of the NND of PI(3,4)P2-AF555 to SON-AF647 with zoom-in to the boxed nuclear speckles. The most frequent (Mode) NND (F) and their fraction (G), Spearman rank correlation (H) and Manders overlap (I) coefficients between PI(3,4)P2 and SON, Rand. Rotated and Rand. Generated SON. Cross-correlation (CC) intensities of the real (J) Rand. Rotated (K) and Rand. Generated (L) PI(3,4)P2-SON. PI(3,4)P2-AF555 (M) and RNAPII-AF647 (N) imaged by dSTORM and visualized as normalized Gaussian fit of thePSF into the individual localizations, merged image (O) and zoom-in to the boxed regions (1, 2). (P) Distribution of the Global and Local NND between PI(3,4)P2-AF555 and RNAPII-AF647 in the real (PI(3,4)P2-RNAPII), randomized by rotation (Rand. Rotated) or randomly generated (Rand. Generated) images. (Q) Color-coded pixel map of the NND of PI(3,4)P2-AF555 to RNAPII-AF647 with zoom-in to the boxed regions (1, 2). The most frequent (Mode) NND (R) and their fraction (S), Spearman rank correlation (T) and Manders overlap (U) coefficients between PI(3,4)P2-SON, Rand. Rotated and Rand. Generated RNAPII. Cross-correlation (CC) intensities of the real (V) Rand. Rotated (W) and Rand. Generated (Z) PI(3,4)P2-AF555 and RNAPII–AF647. Scale bars = 5 μm; 1 μm in the zoom-in images and 50 nm in the CC visualization. Calibration bar shows the relative level of CC.

0.02 and in the case of rand. generated was almost completely diminished ($P < 0.005$; $N = 8$) to 0.001 ± 0.001 (Fig. 5H). The overlap of Voronoi polygons surrounding PI(3,4)P2-AF555 and SON-AF647 SMLs was characterized by Manders coefficient 0.51 ± 0.09, which was ~7.3-fold reduced ($P < 0.005$; $N = 8$) for rand. rotated SMLs to 0.07 ± 0.01 and ~13-fold reduced ($P < 0.005$; $N = 8$) in the case of rand. generated SMLs to 0.04 ± 0.01 (Fig. 5I). Taken together, the NND, Spearman and Manders analyses quantitatively document the non-random co-distribution of PI(3,4)P2 with the nuclear speckle marker SON. These results are further supported and visually documented by the CC analyses (Fig. 5J–L). Sharply centered CC intensities of the real representative image (Fig. 5J) indicate the strong CC between PI(3,4)P2-AF555 and SON-AF647, which is in contrast to the scattered CC intensities that indicate reduced CC between PI(3,4)P2-AF555 and randomly distributed SON-AF647 in the case of the representative rand. rotated (Fig. 5K) and even more of the rand. generated image (Fig. 5L).

Furthermore, we investigated in detail the spatial relationship between PI(3,4)P2-AF555 (Fig. 5M) and RNAPII-AF647 (Fig. 5N). From the real (Fig. 5M–O), rand. rotated (Suppl. Fig. 4E) and rand. generated (Suppl. Fig. 4F) SMLs of PI(3,4)P2-AF555 and RNAPII-AF647 we calculated the NND distributions (Fig. 5P). The color-coded pixel map calculated from the real NND of PI(3,4)P2-AF555 to RNAP-AF647 shows the close proximity of PI(3,4)P2 and RNAPII foci (Fig. 5Q) and this spatial relationship was disrupted in the rand. rotated (Suppl. Fig. 4G) and even more in the rand. generated (Suppl. Fig. 4H) images. From the NND distributions we calculated the mode of the real PI(3,4)P2-AF555 to RNAP-AF647 NND 5.3 ± 0.2 nm, which was ~22% increased ($P < 0.01$; $N = 6$) to 6.5 ± 0.2 nm for the rand. rotated and ~38% increased ($P < 0.05$; $N = 6$) to 7.3 ± 0.2 nm for the rand. generated SMLs (Fig. 5R). The fraction of the NND at the mode NND of the real SMLs was 9 ± 0.2% and this was ~40% reduced ($P < 0.005$; $N = 6$) to 6.4 ± 0.1% for the rand. rotated but not affected for the rand. generated SMLs ($N = 6$), where it was 9.1 ± 0.3% (Fig. 5S).

The correlation of PI(3,4)P2-AF555 with RNAPII-AF647 was characterized by Spearman coefficient 0.14 ± 0.03, which was ~3.5-fold reduced ($P < 0.005$; $N = 6$) in the case of rand. rotated SMLs to 0.04 ±

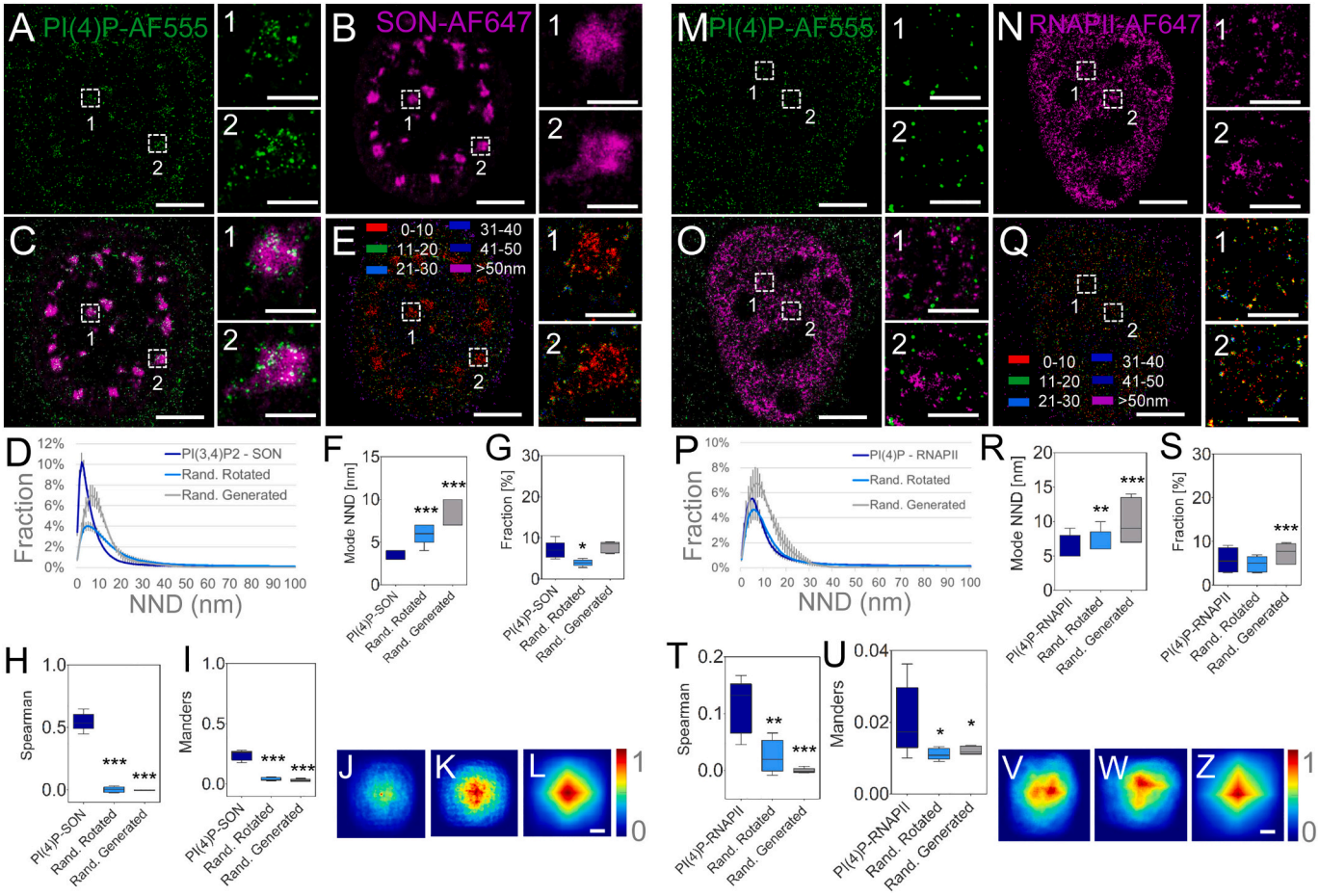

Fig. 6. dSTORM imaging and distribution analysis of PI(4)P with respect to the nuclear speckle marker SON and RNAPII. PI(4)P-AF555 (A) and SON-AF647 (B) imaged by dSTORM and visualized as normalized Gaussian fit of the point spread function (PSF) into the individual localizations, merged image (C) and zoom-in to the boxed nuclear speckles. (D) Distribution of the Global and Local NND between PI(4)P-AF555 and SON-AF647 in the real (PI(4)P-SON), randomized by rotation (Rand. Rotated) or randomly generated (Rand. Generated) images. (E) Color-coded pixel map of the NND of PI(4)P-AF555 to SON-AF647 with zoom-in to the boxed speckles (1, 2). The most frequent (Mode) NND (F) and their fraction (G), Spearman rank correlation (H) and Manders overlap (I) coefficients between PI(4)P and SON, Rand. Rotated or Rand. Generated SON. Cross-correlation (CC) intensities of the real (J) Rand. Rotated (K) and Rand. Generated (L) PI(4)P-AF555 and SON–AF647. PI(4)P-AF555 (M) and RNAPII-AF647 (N) imaged by dSTORM and visualized as normalized Gaussian fit of the PSF into the individual localizations, merged image (O) and zoom-in to the boxed regions (1, 2). (P) Distribution of the Global and Local NND between PI(4)P-AF555 and RNAPII-AF647 in the real (PI(4)P-RNAPII), randomized by rotation (Rand. Rotated) or randomly generated (Rand. Generated) images. (Q) Color-coded pixel map of the NND of PI(4)P-AF555 to RNAPII-AF647 with zoom-in to the boxed regions (1, 2). The most frequent (Mode) NND (R) and their fraction (S), Spearman rank correlation (T) and Manders overlap (U) coefficients between PI(4)P and SON, Rand. Rotated and Rand. Generated RNAPII. Cross-correlation (CC) intensities of the real (V) Rand. Rotated (W) and Rand. Generated (Z) PI(4)P-AF555 and RNAPII–AF647. Scale bars = 5 μm; 1 μm in the zoom-in images and 50 nm in the CC visualization. The calibration bar shows the relative level of CC.

0.01 and in the case of rand. generated was reduced to 0 ($P < 0.005$; $N = 6$) (Fig. 5T). The overlap of between PI(3,4)P2-AF555 and RNAPII-AF647 was characterized by Manders coefficient 0.06 ± 0.01, which was 50% reduced ($P < 0.01$; $N = 6$) for rand. rotated SMLs to 0.04 ± 0.01 and ~3-fold reduced ($P < 0.005$; $N = 6$) to 0.02 ± 0.01 in the case of rand. generated SMLs (Fig. 5U). Despite the small Manders overlap coefficient, although significantly reduced by randomization, the NND analysis together with Spearman correlation suggests the non-random co-distribution of PI(3,4)P2 in the close proximity of a subset of RNAPII foci. This conclusion is also documented by the centered PI(3,4)P2-AF555 and RNAPII-AF647 CC intensities of the real representative image (Fig. 5V) that are slightly more scattered in the case of rand. rotated RNAPII-AF647 SMLs (Fig. 5W) and even more scattered in the case of rand. generated SMLs (Fig. 5Z).

3.6. Nuclear PI(4)P localizes predominantly to the nuclear speckles

PI(4)P2 is the precursor for the biosynthesis of PI(3,4)P2 and PI(4,5)P2 and despite the greater abundance of PI(4)P in the cytoplasm, it also localizes to the cell nucleus [19,24]. Therefore, the detailed information about the nuclear localization PI(4)P with respect to PI(4,5)P2 and PI(3,4)P2 is a relevant for better understanding of the metabolism and signaling roles of nuclear PIPs. In the cell nucleus, we observed the PI(4)P signal concentrated in sub-nuclear regions and scattered in the nucleoplasm (Fig. 6). This was reminiscent of PI(4,5)P2 (Figs. 1–3) and PI(3,4)P2 (Fig. 5) but with a much lower abundance of PI(4)P compared to PI(4,5)P2 and PI(3,4)P2. Dual-color dSTORM imaging of PI(4)P2-AF555 (Fig. 6A) and the nuclear speckle marker SON-AF647 (Fig. 6B) showed PI(4)P-AF555 dispersed within the SON matrix (Fig. 6C), similarly to PI(4,5)P2 (Fig. 2C) and PI(3,4)P2 (Fig. 5C). We calculated normalized NND distributions between the real, rand. rotated (Suppl. Fig. 5A) and rand. generated (Suppl. Fig. 5B). This proximity was diminished in the rand. rotated (Suppl. Fig. 5C) and rand. generated (Suppl. Fig. 5D) SMLs. PI(4)P-AF555 and SON-AF647 SMLs (Fig. 6D). The color-coded pixel map calculated from the PI(4)P-AF555 to SON-AF647 NNDs shows the close proximity of PI(4)P to SON in the nuclear speckles (Fig. 6E). From the NND distributions, we calculated the mode NND of 3.6 ± 0.2 nm, which was increased ~67% ($P < 0.005$; $N = 5$) for the rand. rotated SON-AF647 SMLs to 6 ± 0.4 nm and ~2.3-fold increased ($P < 0.005$; $N = 5$) to 8.2 ± 0.5 nm (Fig. 6F) for the rand. generated SON-AF647 SMLs. The fraction of the NND at the mode NND was 7 ± 0.6% and this was ~44% reduced ($P < 0.05$; $N = 5$) to 3.9 ± 0.2% for the rand. rotated SMLs but not significantly affected for rand. generated SMLs, where it was 7.8 ± 0.4% (Fig. 6G).

The correlation of PI(4)P-AF555 with SON-AF647 was characterized by Spearman coefficient 0.54 ± 0.03, which was greatly reduced ($P < 0.005$; $N = 5$) in the case of rand. rotated SON-AF647 SMLs to 0.002 ± 0.001 and to 0 ($P < 0.005$; $N = 5$) in the case of rand. generated SON-AF647 SMLs (Fig. 6H). The overlap of Voronoi polygons surrounding PI(4)P-AF555 and SON-AF647 SMLs was characterized by Manders coefficient 0.24 ± 0.02, which was ~6-fold reduced ($P < 0.005$; $N = 5$) for rand. rotated SMLs to 0.04 ± 0.01 and ~8-fold reduced ($P < 0.005$; $N = 5$) in the case of rand. generated SMLs to 0.03 ± 0.01 (Fig. 6I). The lower Manders overlap of PI(4)P-AF555 and SON-AF647 in comparison to Manders overlaps of PI(4,5)2P-AF555 and PI(3,4)P2-AF555 with SON-AF647 reflects the lower abundance of PI(4)P-AF555 compared to the abundances of PI(4,5)2P-AF555 and PI(3,4)P2-AF555. Sharply centered PI(4)P-AF555 to SON-AF647 CC intensities of the real representative image (Fig. 6J) indicate strong CC between PI(4)P-AF555 and SON-AF647 that strongly contrasts with the scattered CC intensities of the randomized images (Fig. 5K, L). This indicates reduced CC of PI(4)P2-AF555 with rand. rotated and rand. generated SON-AF647. Taken together, these quantitative analyses collectively indicate the non-random co-distribution of PI(4)P with the nuclear speckle marker SON.

Furthermore, we investigated in detail the spatial relationship between PI(4)P-AF555 (Fig. 6M) and RNAPII-AF647 (Fig. 6N). From the real PI(4)P-AF555 and RNAPII-AF647 (Fig. 6O) data, rand. rotated (Suppl. Fig. 5E) and rand. generated (Suppl. Fig. 5F) data we calculated the normalized NND distributions (Fig. 6P). The color-coded pixel map of the NND of PI(4)P-AF555 to RNAP-AF647 suggest very little co-clustering of PI(4)P2 with RNAPII (Fig. 6Q), similarly to the NND map of PI(4)P-AF555 to rand. rotated (Suppl. Fig. 5G) and rand. generated (Suppl. Fig. 5H) RNAPII-AF647. From the NND distributions we calculated the mode NND 6.2 ± 0.5 nm between the real PI(4)P2-AF555 to RNAP-AF647 NND, which was ~12% increased ($P < 0.01$; $N = 5$) to 7 ± 0.5 nm for the rand. rotated and ~61% increased ($P < 0.005$; $N = 5$) to 10 ± 1 nm for the rand. generated SMLs (Fig. 6R). The fraction of the NND at the mode NND of the real SMLs was 5.7 ± 0.8% and this was not significantly reduced ($N = 5$) to 4.8 ± 0.5% for the rand. rotated but increased ~28% ($P < 0.005$; $N = 5$) to 7.3 ± 0.8% for the rand. generated SMLs (Fig. 6S).

The NND analysis suggested that the level of co-patterning between PI(4)P and RNAPII is lower compared to the co-patterning of PI(4,5)P2 and PI(3,4)P2 with RNAPII. This conclusion was further supported by the correlation and overlap analyses of PI(4)P-AF555 and RNAPII-AF647. The Spearman correlation coefficient of PI(4)P-AF555 with the real RNAPII-AF647 SMLs was 0.11 ± 0.02 and it was reduced more than 5-fold ($P < 0.005$; $N = 5$) for rand. rotated RNAPII-AF647 SMLs and reduced to 0 ($P < 0.005$; $N = 5$) for rand. generated RNAPII-AF647 SMLs. The overlap between PI(4)P2-AF555 and RNAPII-AF647 was characterized by Manders coefficient 0.02 ± 0.004, which was about a half-reduced for both, rand. rotated and rand. generated RNAPII-AF647 SMLs, to 0.01 ± 0.001 and 0.012 ± 0.0005 ($P < 0.05$; $N = 5$ for both), resp. These data are further supported by the scattered CC intensities between the real PI(4)P-AF555 and RNAPII-AF647 (Fig. 6V), which indicate low or no CC, similarly to the CC of rand. rotated (Fig. 6W) and rand. generated RNAPII-AF647 SMLs (Fig. 6Z). Taken together, our quantitative analyses suggest that nuclear PI(4)P concentrates predominantly in the nuclear speckles, where it could enter a biosynthesis pathway of PI(4,5)P2 and PI(3,4)P2. In contrast to PI(4,5)P2 and PI(3,4)P2, PI(4)P does not display conclusive proximity to the RNAPII foci.

4. Discussion

The models that were developed using SMLM acknowledge protein clustering and the formation of transcriptional condensates as the driving force of gene expression [54,62–65]. However, those models largely overlook the role of nuclear lipids and particularly the nuclear PIPs. Biochemical characterization of the PIP functions at different nuclear compartments is limited by the difficulties connected with the isolation and subsequent fractionation of these compartments. Albeit a comprehensive mass-spectrometry analysis of the human nuclear PI(4,5)P2-interactors has been recently performed [7], the spatiotemporal context of the PIP function is typically lost during classical biochemical analyses. Therefore, here we have for the first time resolved at the nanoscale the spatial distribution of three nuclear PIPs, the most abundant nuclear PIP - PI(4,5)P2, then PI(3,4)P2, and their biosynthetic precursor PI(4)P, within sub-nuclear compartments. We quantitatively characterized their spatial relationship with the nuclear speckle marker SON, with RNAPII and with nucleolar Fib. We performed the distance analyses by ImageJ2 [60] plug-in ThunderSTORM [61] and co-distribution analyses by CT [59]. The NND calculation by ThunderSTORM was previously used to confirm the co-localization analysis of the confocal microscopy data by the nanoscale separation of the transcription and replication sites in the nucleoli [58]. Here we extended the NND analysis and calculated from the normalized NND distributions two parameters: the mode (most frequent) NND and the fraction of NND at the mode NND (Suppl. Table 1). We chose mode over mean or median because we preferred to evaluate the shift of the NND distribution peaks as a measure of the spatial relationship between SMLs of PIPs and the respective markers. We developed a visualization tool that creates images in which pixels are color-coded based on the NND of one probe

(PIP) in respect to the second probe (SON, RNAPII, Fib). This tool, which we developed for the practical visualization of the spatial distribution of PIPs *in-cellulo* and for the better understanding of the PIP role in the establishment of the functional nuclear architecture, is applicable in the further studies of the spatial organization of the cell nucleus. Second parameter that we devised from the NND analysis was the fraction of neighbors at the mode NND, which represents the relative amount of the most frequent pair-wise NNDs [57]. Dunn et al. [56] suggested the randomization of the experimental data by rotating one channel of the dual-color image and comparing the spatial relationship between two channels in the real and randomized data. We modified this approach and randomized the data by swapping the x and y coordinates of the SMLs of SON, RNAPII and Fib. In addition, we generated random SMLs with the same density as the respective marker by ThunderSTORM. Using these two randomization approaches we quantitatively showed that all three studied PIPs co-pattern with SON; PI(4,5)P2 and PI(3,4)P2 with RNAPII; and PI(4,5)P2 also with Fib. Although randomization by rotation and randomly generated SMLs had an increasing effect on the NND between all three investigated PIPs and all respective markers, randomly generated SMLs increased in all cases NND more than randomization by rotation (Suppl. Table 2). Randomization by rotation reduced the fraction of NNDs at the mode NND in all cases (except for PI(4)P2-RNAPII; see below) but randomly generated SMLs only rarely reduced the fraction of NNDs at the mode NND. This is given by the fact that randomization by rotation led to the reduced peak and increased tail of NND distributions to larger NNDs, while randomly distributed SMLs with the same density as was the real SML density of the respective marker resulted in the NND distribution similar to the real data but with peaks (mode) shifted to larger NNDs. Importantly, rand. generated SMLs led to the much greater disruption of Spearman correlation and Manders overlap than the rand. rotated data. Therefore, although rand. rotation is a faster method, rand. generated SMLs are more rigorous for the quantitative evaluation of the co-patterning in the real data. This is especially important for the dispersed and/or dense SMLs such as RNAPII or for the patterns with the specific geometry, such as Fib.

Spearman correlation coefficients of PI(4,5)P2, PI(3,4)P2 and PI(4)P with RNAPII were in the similar range (0.13 ± 0.01, 0.14 ± 0.03 and 0.11 ± 0.02, resp.), which would indicate the correlation of a small subset of the respective PIPs with RNAPII foci. However, Manders overlap coefficient of PI(4,5)P2 with RNAPII (0.15 ± 0.01) was more than twice and almost a magnitude greater compared to PI(3,4)P2 (0.06 ± 0.01) and PI(4)P (0.02 ± 0.004), resp. The overall low level of Manders overlap is given by the sub-diffraction limited size of PIP and RNAPII foci, which at the nanoscale level do not largely overlap but rather localize in close proximity to each other. This suggests that those parameters alone are not satisfactory for the conclusive evaluation of the spatial relationship between dispersed signals of PIPs and RNAPII at the nanoscale. Therefore, we combined CT with the NND analysis. The mode NND between PI(4)P and RNAPII (6.2 ± 0.5 nm) is greater than that of PI(4,5)P2 (5.6 ± 0.2 nm) or PI(3,4)P2 (5.3 ± 0.2 nm) and RNAPII. Similarly, the fraction of the NND at the mode NND is lower in the case of PI(4)P-RNAPII (5.7 ± 0.8%) compared to PI(4,5)P2-RNAPII (7.6 ± 0.6%) and PI(3,4)P2-RNAPII (9 ± 0.2%). In the case of PI(4,5)P2 and PI(3,4)P2 co-patterning with RNAPII, randomization by rotation reduced the fraction of NNDs at the mode NND, while the randomly generated distribution of SMLs did not affect this parameter in these two instances. In contrast, for PI(4)P-RNAPII co-patterning, randomization by rotation did not affect the fraction of NNDs at the mode NND, while randomly generated distribution of RNAPII-AF647 SMLs increased the fraction of NNDs at the mode NND. Therefore we suggest that PI(4,5)P2 and PI(3,4)P2, in contrary to PI(4)P, display specific co-patterning with RNAPII (Fig. 7). Nucleoplasmic PI(4,5)P2 pool was previously localized to the periphery of the nuclear lipid isles (NLIs), where it interacts with the RNAPII transcription machinery [22]. The important question is whether NLIs might be building blocks for the nuclear speckles and/or perhaps also nucleoli and whether NLIs are eventually dynamic

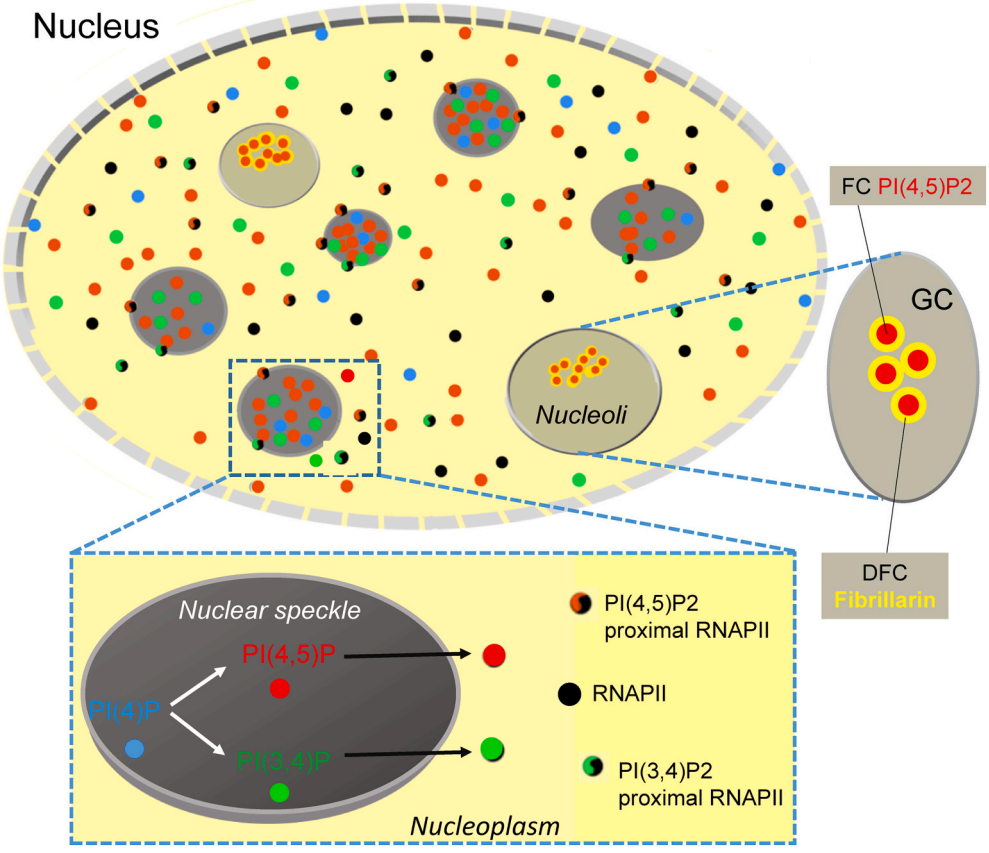

Fig. 7. Detailed map of the sub-nuclear localization of PI(4,5)P2, PI(3,4)P2 and PI(4)P. All three phosphatidylinositol phosphates (PIPs) localize to the nucleoplasm, but only PI(3,4)P2 and PI(4,5)P2 are proximal to the subset of RNAPII foci. All three PIPs (as well as their biosynthetic enzymes) localize to the nuclear speckles, which could therefore represent a hub for the PIP metabolism. PI(4,5)P2 localizes to the nucleolar fibrillar center (FC) and is surrounded by fibrillarin that localizes to the dense fibrillar component (DFC).

structures that regulate the distribution of RNAPII and possibly also of RNA polymerase I. Accumulating evidence based on the previous work [7] and our present data suggest the role of PIPs as a localization signal that orchestrates nuclear functions in addition to its regulatory role for the enzymatic functions of PIP-interacting proteins, such as Fib, poly(A) polymerase, RNAPII or PHF8 [8,9,22,23]. RNAPII was previously localized to the small foci in the nucleoplasm by SMLM [54,63–65] and to the periphery of nuclear speckles by confocal microscopy [35] and was found to overlap with the signal of nucleoplasmic PI(4,5)P2 by SIM [22]. However, the relationship of PI(4,5)P2 with RNAPII has not been previously quantitatively characterized in the details and the role of PIPs in the regulation of gene expression only starts to emerge [9,22,23]. Here we provide novel evidence for the association of at least a subset of nucleoplasmic PI(3,4)P2 with RNAPII foci. Those data further support the proposed role of PIPs in the orchestration of RNAPII transcription [4,22]. We uncovered with nanoscale resolution the matrix-like structure of the nuclear speckle marker SON and localization of PI(4)P, PI(3,4)P2 and PI(4,5)P2 within the SON matrix. This is in agreement with the localization to the nuclear speckles of the enzymes PI3KCα, PIP5KIα and PIP5KIγ_i4 that catalyze the biosynthesis of PI(3,4)P2 and PI(4,5)P2 from PI(4)P [3,9,17,18,20,26]. The nuclear speckle organization is established by the interactions between RNA and proteins that can be described by a coarse-grained model [39,66]. In this model, the spatial organization arises from the different affinities between RNA and proteins in comparison to their affinities for the solvent. The equilibrium of the interactions between the polymer (RNA or protein) with solvent and the polymers with each other results in the matrix organization of membrane-less compartments. This process could in theory lead to the localization of PIPs within the caveats of the matrix such as created by SON, which would protect hydrophobic acyl chains from the neighboring aqueous solution. This speculation is in line with the notion of the nuclear speckles having a sponge-like structure and the density lower than that of the surrounding nucleoplasm [67]. Taken together, it is plausible to envision a scenario in which nuclear speckles represent hubs of nuclear PIP metabolism (Fig. 7). Therefore, our data are therefore relevant for a better understanding of the role of nuclear speckles in the metabolism of PIPs. The nucleolar PI(4,5)P2 represents only a small fraction of the total nuclear PI(4,5)P2.

Earlier we have shown by confocal and by electron microscopy the co-localization and co-clustering of the nucleolar Fib in the DFC with the nucleolar PI(4,5)P2 localized mainly in the FC or at the FC/DFC interface [10,11]. Nucleolar Fib was recently shown by SIM to surround the nucleolar PI(4,5)P2, which regulates the RNAse activity of Fib [8]. Here we bridged the gap between confocal and electron microscopy, recapitulated, further resolved in greater detail and quantitatively characterized the localization of PI(4,5)P2 within Fib structures that appear almost symmetrically organized around nucleolar PI(4,5)P2. We reached by SMLM the localization level previously set by electron tomography [11] and provided for the first time the detailed quantitative analyses of the spatial relationship between nucleolar PI(4,5)P2 and Fib, which is relevant for a better understanding of the role of PI(4,5)P2 in the nucleoli.

In summary, our systematic analyses of the nuclear PI(4,5)P2, PI(3,4)P2 and PI(4)P localization within nuclear speckles, nucleoplasm and nucleoli provide the map of the spatial distribution of nuclear PIPs with nanometer resolution. Our present data are in agreement with the proposed role of the nuclear PIPs in the formation of lipo-ribonucleoprotein hubs and relevant for a better understanding of the role of nuclear PIPs in health and disease [5,68,69]. Discussed in-depth data evaluation provides the experimental workflow applicable for the subsequent imaging studies of different nuclear PIPs and their effectors. The availability to the researchers from the field of nuclear lipid biology, who routinely use the combination of biochemistry and lipidomics, will broaden their studies by the precise *in cellulo* localization approaches. Therefore, our experimental guidelines that combine SMLM with rigorous quantitative analysis provide a complementary tool to the biochemical analyses for the evaluation of PIP functions in the compartmentalization of nuclear processes.

Funding

We acknowledge Imaging Methods Core Facility at BIOCEV, institution supported by the Ministry of Education, Youth and Sports, Czechia (MEYS CR; Large RI Project LM2018129 Czech-BioImaging) and European Regional Development Fund (ERDF; project No. CZ.02.1.01/0.0/0.0/16_013/0001775) for their support. Microscopy was performed in the Laboratory of Confocal and Fluorescence Microscopy co-financed by the ERDF and the state budget of the Czech Republic, projects no. CZ.1.05/4.1.00/16.0347 and CZ.2.16/3.1.00/21515, and supported by the Czech-BioImaging large RI project LM2018129. This work was supported by the Grant Agency of the Czech Republic (grant nos. 19-05608S and 18-19714S); by the Czech Academy of Sciences (grant no. JSPS-20-06); by the Institutional Research Concept of the Institute of Molecular Genetics (grant no. RVO: 68378050); and by the MEYS CR (COST Inter-excellence internship LTC19048 and LTC20024 and Action 15214 EuroCellnet) and BIOCEV – Biotechnology and Biomedicine Centre of the Academy of Sciences and Charles University (CZ.1.05/1.1.00/02.0109).

CRediT authorship contribution statement

Pe. H. conceptualization, investigation, methodology, analysis, data curation, validation, visualization, original and revised manuscript writing; O. Š. software, visualization. M. Sch. analysis, data curation, visualization; E. C. conceptualization, material contribution, revised manuscript writing; M. Sz. conceptualization, analysis, data curation, validation, visualization, original and revised manuscript writing; Pa. H. supervision, funding, conceptualization, original and revised manuscript writing.

Declaration of competing interest

The authors declare that they have no known competing financial interests or personal relationships that could have appeared to influence the work reported in this paper.

Acknowledgments

We are grateful to Marie Olšinova and Aleš Benda for their initial help with microscopy, to Zdeněk Švindrych for the advice with ThunderSTORM, to Ana Miladinović for the evaluation of anti-PI(3,4)P2 antibody, to Lenka Pišlová for her excellent administrative assistance, to Iva Jelínková for her assistance with the cell cultures and Pavel Kříž for the lab management.

Appendix A. Supplementary data

Supplementary data to this article can be found online at https://doi.org/10.1016/j.bbalip.2021.158890.

References

[1] T. Balla, Phosphoinositides: tiny lipids with giant impact on cell regulation, Physiol. Rev. 93 (3) (2013) 1019–1137, https://doi.org/10.1152/physrev.00028.2012.
[2] G. Di Paolo, P. De Camilli, Phosphoinositides in cell regulation and membrane dynamics, Nature 443 (7112) (2006) 651–657, https://doi.org/10.1038/nature05185.
[3] M.W. Bunce, K. Bergendahl, R.A. Anderson, Nuclear PI(4,5)P(2): a new place for an old signal, Biochim. Biophys. Acta 1761 (5–6) (2006) 560–569, https://doi.org/10.1016/j.bbalip.2006.03.002.
[4] E. Castano, S. Yildirim, V. Faberova, A. Krausova, L. Ulicna, D. Paprckova, P. Hozak, Nuclear phosphoinositides-Versatile Regulators of Genome Functions, Cells 8 (7) (2019), https://doi.org/10.3390/cells8070649.

[5] M. Sztacho, M. Sobol, C. Balaban, S.E. Escudeiro Lopes, P. Hozak, Nuclear phosphoinositides and phase separation: important players in nuclear compartmentalization, Adv Biol Regul 71 (2019) 111–117, https://doi.org/10.1016/j.jbior.2018.09.009.

[6] A.E. Lewis, L. Sommer, M. Arntzen, Y. Strahm, N.A. Morrice, N. Divecha, C. S. D'Santos, Identification of nuclear phosphatidylinositol 4,5-bisphosphate-interacting proteins by neomycin extraction, Mol Cell Proteomics 10 (2) (Feb 2011), M110.003376, https://doi.org/10.1074/mcp.M110.003376 (Epub 2010 Nov 3. PMID: 21048195; PMCID: PMC3033679).

[7] M. Sztacho, B. Šalovská, J. Červenka, C. Balaban, P. Hoboth, P. Hozák, Limited proteolysis-coupled mass spectrometry identifies phosphatidylinositol 4,5-bisphosphate effectors in human nuclear proteome, Cells. 10 (1) (Jan 4 2021), E68, https://doi.org/10.3390/cells10010068. 33406800.

[8] F. Guillen-Chable, U.R. Corona, A. Pereira-Santana, A. Bayona, L.C. Rodriguez-Zapata, C. Aquino, E. Castano, Fibrillarin Ribonuclease Activity is Dependent on the GAR Domain and Modulated by Phospholipids, Cells 9 (5) (2020), https://doi.org/10.3390/cells9051143.

[9] D.L. Mellman, M.L. Gonzales, C. Song, C.A. Barlow, P. Wang, C. Kendziorski, R. A. Anderson, A PtdIns4,5P2-regulated nuclear poly(A) polymerase controls expression of select mRNAs, Nature 451 (7181) (2008) 1013–1017, https://doi.org/10.1038/nature06666.

[10] M. Sobol, S. Yildirim, V.V. Philimonenko, P. Marasek, E. Castano, P. Hozak, UBF complexes with phosphatidylinositol 4,5-bisphosphate in nucleolar organizer regions regardless of ongoing RNA polymerase I activity, Nucleus 4 (6) (2013) 478–486, https://doi.org/10.4161/nucl.27154.

[11] S. Yildirim, E. Castano, M. Sobol, V.V. Philimonenko, R. Dzijak, T. Venit, P. Hozak, Involvement of phosphatidylinositol 4,5-bisphosphate in RNA polymerase I transcription, J. Cell Sci. 126 (Pt 12) (2013) 2730–2739, https://doi.org/10.1242/jcs.123661.

[12] J.D. York, A.R. Odom, R. Murphy, E.B. Ives, S.R. Wente, A phospholipase C-dependent inositol polyphosphate kinase pathway required for efficient messenger RNA export, Science. 285 (5424) (1999 Jul 2) 96–100, https://doi.org/10.1126/science.285.5424.96. 10390371.

[13] K. Zhao, W. Wang, O.J. Rando, Y. Xue, K. Swiderek, A. Kuo, G.R. Crabtree, Rapid and phosphoinositol-dependent binding of the SWI/SNF-like BAF complex to chromatin after T lymphocyte receptor signaling, Cell. 95 (5) (Nov 25 1998) 625–636, https://doi.org/10.1016/s0092-8674(00)81633-5 (PMID: 9845365).

[14] Cocco L, Gilmour RS, Ognibene A, Letcher AJ, Manzoli FA, Irvine RF. Synthesis of polyphosphoinositides in nuclei of Friend cells. Evidence for polyphosphoinositide metabolism inside the nucleus which changes with cell differentiation. Biochem J. Dec 15 1987;248(3):765–70. doi: https://doi.org/10.1042/bj2480765. (PMID: 2829840; PMCID: PMC1148615).

[15] G. Hammond, C.L. Thomas, G. Schiavo, Nuclear phosphoinositides and their functions, Curr. Top. Microbiol. Immunol. 282 (2004) 177–206, https://doi.org/10.1007/978-3-642-18805-3_7.

[16] R.F. Irvine, Nuclear lipid signalling, Nat Rev Mol Cell Biol 4 (5) (2003) 349–360, https://doi.org/10.1038/nrm1100.

[17] S.A. Didichenko, M. Thelen, Phosphatidylinositol 3-kinase c2alpha contains a nuclear localization sequence and associates with nuclear speckles, J. Biol. Chem. 276 (51) (Dec 21 2001) 48135–48142, https://doi.org/10.1074/jbc.M104610200. Epub 2001 Oct 17, 11606566.

[18] N.J. Schill, R.A. Anderson, Two novel phosphatidylinositol-4-phosphate 5-kinase type Igamma splice variants expressed in human cells display distinctive cellular targeting, Biochem J. 422 (3) (Aug 27 2009) 473–482, https://doi.org/10.1042/BJ20090638 (PMID: 19548880; PMCID: PMC2782315).

[19] V. Faberova, I. Kalasova, A. Krausova, P. Hozak, Super-resolution localisation of nuclear PI(4)P and identification of its interacting proteome, Cells 9 (5) (2020), https://doi.org/10.3390/cells9051191.

[20] S.L. Osborne, C.L. Thomas, S. Gschmeissner, G. Schiavo, Nuclear PtdIns(4,5)P2 assembles in a mitotically regulated particle involved in pre-mRNA splicing, J. Cell Sci. 114 (Pt 13) (2001) 2501–2511.

[21] B. Payrastre, M. Nievers, J. Boonstra, M. Breton, A.J. Verkleij, Van Bergen en Henegouwen, P. M., A differential location of phosphoinositide kinases, diacylglycerol kinase, and phospholipase C in the nuclear matrix, J. Biol. Chem. 267 (8) (1992) 5078–5084.

[22] M. Sobol, A. Krausova, S. Yildirim, I. Kalasova, V. Faberova, V. Vrkoslav, P. Hozak, Nuclear phosphatidylinositol 4,5-bisphosphate islets contribute to efficient RNA polymerase II-dependent transcription, J Cell Sci 131 (8) (2018), https://doi.org/10.1242/jcs.211094.

[23] L. Ulicna, A. Kalendova, I. Kalasova, T. Vacik, P. Hozak, PIP2 epigenetically represses rRNA genes transcription interacting with PHF8, Biochim. Biophys. Acta Mol. Cell Biol. Lipids 1863 (3) (2018) 266–275, https://doi.org/10.1016/j.bbalip.2017.12.008.

[24] I. Kalasova, V. Fáberová, A. Kalendová, S. Yildirim, L. Uličná, T. Venit, P. Hozák, Tools for visualization of phosphoinositides in the cell nucleus, Histochem. Cell Biol. 145 (4) (Apr 2016) 485–496, https://doi.org/10.1007/s00418-016-1409-8. Epub 2016 Feb 4, 26847181.

[25] Á. Román-Fernández, J. Roignot, E. Sandilands, M. Nacke, M.A. Mansour, L. McGarry, E. Shanks, K.E. Mostov, D.M. Bryant, The phospholipid PI(3,4)P_2 is an apical identity determinant, Nat Commun. 9 (1) (Nov 28 2018) 5041, https://doi.org/10.1038/s41467-018-07464-8 (PMID: 30487552; PMCID: PMC6262019).

[26] I.V. Boronenkov, J.C. Loijens, M. Umeda, R.A. Anderson, Phosphoinositide signaling pathways in nuclei are associated with nuclear speckles containing pre-mRNA processing factors, Mol. Biol. Cell 9 (12) (1998) 3547–3560, https://doi.org/10.1091/mbc.9.12.3547.

[27] M. Thiry, Differential location of nucleic acids within interchromatin granule clusters, Eur. J. Cell Biol. 62 (2) (1993) 259–269.

[28] K.C. Carter, D. Bowman, W. Carrington, K. Fogarty, J.A. McNeil, F.S. Fay, J. B. Lawrence, A three-dimensional view of precursor messenger RNA metabolism within the mammalian nucleus, Science 259 (5099) (1993) 1330–1335, https://doi.org/10.1126/science.8446902.

[29] K.C. Carter, K.L. Taneja, J.B. Lawrence, Discrete nuclear domains of poly(A) RNA and their relationship to the functional organization of the nucleus, J. Cell Biol. 115 (5) (1991) 1191–1202, https://doi.org/10.1083/jcb.115.5.1191.

[30] L.L. Hall, K.P. Smith, M. Byron, J.B. Lawrence, Molecular anatomy of a speckle, Anat Rec A Discov Mol Cell Evol Biol 288 (7) (2006) 664–675, https://doi.org/10.1002/ar.a.20336.

[31] D.L. Spector, X.D. Fu, T. Maniatis, Associations between distinct pre-mRNA splicing components and the cell nucleus, EMBO J. 10 (11) (1991) 3467–3481.

[32] D.L. Spector, A.I. Lamond, Nuclear speckles, Cold Spring Harb. Perspect. Biol. 3 (2) (2011), https://doi.org/10.1101/cshperspect.a000646.

[33] Y. Chen, A.S. Belmont, Genome organization around nuclear speckles, Curr. Opin. Genet. Dev. 55 (2019) 91–99, https://doi.org/10.1016/j.gde.2019.06.008.

[34] J. Kim, K.Y. Han, N. Khanna, T. Ha, A.S. Belmont, Nuclear speckle fusion via long-range directional motion regulates speckle morphology after transcriptional inhibition, J. Cell Sci. 132 (8) (2019), https://doi.org/10.1242/jcs.226563.

[35] Y. Chen, Y. Zhang, Y. Wang, L. Zhang, E.K. Brinkman, S.A. Adam, A.S. Belmont, Mapping 3D genome organization relative to nuclear compartments using TSA-Seq as a cytological ruler, J Cell Biol 217 (11) (2018) 4025–4048, https://doi.org/10.1083/jcb.201807108.

[36] D. Cazalla, K. Newton, J.F. Caceres, A novel SR-related protein is required for the second step of Pre-mRNA splicing, Mol. Cell. Biol. 25 (8) (2005) 2969–2980, https://doi.org/10.1128/MCB.25.8.2969-2980.2005.

[37] N. Saitoh, C.S. Spahr, S.D. Patterson, P. Bubulya, A.F. Neuwald, D.L. Spector, Proteomic analysis of interchromatin granule clusters, Mol. Biol. Cell 15 (8) (2004) 3876–3890, https://doi.org/10.1091/mbc.e04-03-0253.

[38] A. Sharma, H. Takata, K. Shibahara, A. Bubulya, P.A. Bubulya, Son is essential for nuclear speckle organization and cell cycle progression, Mol. Biol. Cell 21 (4) (2010) 650–663, https://doi.org/10.1091/mbc.E09-02-0126.

[39] J. Fei, M. Jadaliha, T.S. Harmon, I.T.S. Li, B. Hua, Q. Hao, T. Ha, Quantitative analysis of multilayer organization of proteins and RNA in nuclear speckles at super resolution, J Cell Sci 130 (24) (2017) 4180–4192, https://doi.org/10.1242/jcs.206854.

[40] İ.A. Ilik, M. Malszycki, A.K. Lübke, C. Schade, D. Meierhofer, T. Aktaş, SON and SRRM2 are essential for nuclear speckle formation, Elife 9 (Oct 23 2020), e60579, https://doi.org/10.7554/eLife.60579 (PMID: 33095160; PMCID: PMC7671692).

[41] L. Davis, M. Cadrin, D.L. Brown, N. Chaly, Reversible disassembly of transcription domains in lymphocyte nuclei during inhibition of RNA synthesis by DRB, Biol. Cell. 78 (3) (1993) 163–180, https://doi.org/10.1016/0248-4900(93)90127-z.

[42] A.I. Lamond, D.L. Spector, Nuclear speckles: a model for nuclear organelles, Nat Rev Mol Cell Biol 4 (8) (2003) 605–612, https://doi.org/10.1038/nrm1172.

[43] F.M. Boisvert, S. van Koningsbruggen, J. Navascues, A.I. Lamond, The multifunctional nucleolus, Nat Rev Mol Cell Biol 8 (7) (2007) 574–585, https://doi.org/10.1038/nrm2184.

[44] O.V. Iarovaia, E.P. Minina, E.V. Sheval, D. Onichtchouk, S. Dokudovskaya, S. V. Razin, Y.S. Vassetzky, Nucleolus: a central hub for nuclear functions, Trends Cell Biol. 29 (8) (2019) 647–659, https://doi.org/10.1016/j.tcb.2019.04.003.

[45] J. Berry, S.C. Weber, N. Vaidya, M. Haataja, C.P. Brangwynne, RNA transcription modulates phase transition-driven nuclear body assembly, Proc. Natl. Acad. Sci. U. S. A. 112 (38) (2015) E5237–E5245, https://doi.org/10.1073/pnas.1509317112.

[46] D. Hernandez-Verdun, Assembly and disassembly of the nucleolus during the cell cycle, Nucleus 2 (3) (2011) 189–194, https://doi.org/10.4161/nucl.2.3.16246.

[47] D.M. Mitrea, R.W. Kriwacki, Phase separation in biology; functional organization of a higher order, Cell Commun Signal 14 (2016) 1, https://doi.org/10.1186/s12964-015-0125-7.

[48] M.Y. Shubina, Y.R. Musinova, E.V. Sheval, Nucleolar methyltransferase fibrillarin: evolution of structure and functions, Biochemistry (Mosc) 81 (9) (2016) 941–950, https://doi.org/10.1134/S0006297916090030.

[49] M. Heilemann, S. van de Linde, M. Schuttpelz, R. Kasper, B. Seefeldt, A. Mukherjee, M. Sauer, Subdiffraction-resolution fluorescence imaging with conventional fluorescent probes, Angew Chem Int Ed Engl 47 (33) (2008) 6172–6176, https://doi.org/10.1002/anie.200802376.

[50] S. van de Linde, A. Loschberger, T. Klein, M. Heidbreder, S. Wolter, M. Heilemann, M. Sauer, Direct stochastic optical reconstruction microscopy with standard fluorescent probes, Nat. Protoc. 6 (7) (2011) 991–1009, https://doi.org/10.1038/nprot.2011.336.

[51] C. Cremer, A. Szczurek, F. Schock, A. Gourram, U. Birk, Super-resolution microscopy approaches to nuclear nanostructure imaging, Methods. 123 (Jul 1 2017) 11–32, https://doi.org/10.1016/j.ymeth.2017.03.019. Epub 2017 Apr 6, 28390838.

[52] J.B. Grimm, B.P. English, H. Choi, A.K. Muthusamy, B.P. Mehl, P. Dong, L.D. Lavis, Bright photoactivatable fluorophores for single-molecule imaging, Nat Methods 13 (12) (2016) 985–988, https://doi.org/10.1038/nmeth.4034.

[53] M. Gunkel, F. Erdel, K. Rippe, P. Lemmer, R. Kaufmann, C. Hormann, C. Cremer, Dual color localization microscopy of cellular nanostructures, Biotechnol J 4 (6) (2009) 927–938, https://doi.org/10.1002/biot.200900005.

[54] Z.W. Zhao, R. Roy, J.C. Gebhardt, D.M. Suter, A.R. Chapman, X.S. Xie, Spatial organization of RNA polymerase II inside a mammalian cell nucleus revealed by reflected light-sheet superresolution microscopy, Proc. Natl. Acad. Sci. U. S. A. 111 (2) (2014) 681–686, https://doi.org/10.1073/pnas.1318496111.

[55] J.S. Aaron, A.B. Taylor, T.L. Chew, Image co-localization - co-occurrence versus correlation, J. Cell Sci. 131 (3) (2018), https://doi.org/10.1242/jcs.211847.
[56] K.W. Dunn, M.M. Kamocka, J.H. McDonald, A practical guide to evaluating colocalization in biological microscopy, Am J Physiol Cell Physiol 300 (4) (2011) C723–C742, https://doi.org/10.1152/ajpcell.00462.2010.
[57] S. Malkusch, U. Endesfelder, J. Mondry, M. Gelleri, P.J. Verveer, M. Heilemann, Coordinate-based colocalization analysis of single-molecule localization microscopy data, Histochem. Cell Biol. 137 (1) (2012) 1–10, https://doi.org/10.1007/s00418-011-0880-5.
[58] E. Smirnov, J. Borkovec, L. Kovacik, S. Svidenska, A. Schrofel, M. Skalnikova, I. Raska, Separation of replication and transcription domains in nucleoli, J Struct Biol 188 (3) (2014) 259–266, https://doi.org/10.1016/j.jsb.2014.10.001.
[59] F. Levet, G. Julien, R. Galland, C. Butler, A. Beghin, A. Chazeau, J.B. Sibarita, A tessellation-based colocalization analysis approach for single-molecule localization microscopy, Nat Commun 10 (1) (2019) 2379, https://doi.org/10.1038/s41467-019-10007-4.
[60] C.T. Rueden, J. Schindelin, M.C. Hiner, B.E. DeZonia, A.E. Walter, E.T. Arena, K. W. Eliceiri, ImageJ2: ImageJ for the next generation of scientific image data, BMC Bioinformatics 18 (1) (2017) 529, https://doi.org/10.1186/s12859-017-1934-z.
[61] M. Ovesny, P. Krizek, J. Borkovec, Z. Svindrych, G.M. Hagen, ThunderSTORM: a comprehensive ImageJ plug-in for PALM and STORM data analysis and super-resolution imaging, Bioinformatics 30 (16) (2014) 2389–2390, https://doi.org/10.1093/bioinformatics/btu202.
[62] M. Boehning, C. Dugast-Darzacq, M. Rankovic, A.S. Hansen, T. Yu, H. Marie-Nelly, M. Zweckstetter, RNA polymerase II clustering through carboxy-terminal domain phase separation, Nat Struct Mol Biol 25 (9) (2018) 833–840, https://doi.org/10.1038/s41594-018-0112-y.
[63] W.K. Cho, N. Jayanth, B.P. English, T. Inoue, J.O. Andrews, W. Conway, II Cisse, RNA Polymerase II cluster dynamics predict mRNA output in living cells, Elife 5 (2016), https://doi.org/10.7554/eLife.13617.
[64] W.K. Cho, N. Jayanth, S. Mullen, T.H. Tan, Y.J. Jung, I.I. Cisse, Super-resolution imaging of fluorescently labeled, endogenous RNA Polymerase II in living cells with CRISPR/Cas9-mediated gene editing, Sci. Rep. 6 (2016) 35949, https://doi.org/10.1038/srep35949.
[65] W.K. Cho, J.H. Spille, M. Hecht, C. Lee, C. Li, V. Grube, I.I. Cisse, Mediator and RNA polymerase II clusters associate in transcription-dependent condensates, Science 361 (6400) (2018) 412–415, https://doi.org/10.1126/science.aar4199.
[66] M. Feric, N. Vaidya, T.S. Harmon, D.M. Mitrea, L. Zhu, T.M. Richardson, C. P. Brangwynne, Coexisting Liquid Phases Underlie Nucleolar Subcompartments, Cell 165 (7) (2016) 1686–1697, https://doi.org/10.1016/j.cell.2016.04.047.
[67] K.E. Handwerger, J.A. Cordero, J.G. Gall, Cajal bodies, nucleoli, and speckles in the Xenopus oocyte nucleus have a low-density, sponge-like structure, Mol. Biol. Cell 16 (1) (2005) 202–211, https://doi.org/10.1091/mbc.e04-08-0742.
[68] L. Cocco, M.Y. Follo, L. Manzoli, P.G. Suh, Phosphoinositide-specific phospholipase C in health and disease, J Lipid Res. 56 (10) (Oct 2015) 1853–1860, https://doi.org/10.1194/jlr.R057984 (Epub 2015 Mar 27. PMID: 25821234; PMCID: PMC4583093).
[69] A.M. Martelli, R.S. Gilmour, L.M. Neri, L. Manzoli, A.N. Corps, L. Cocco, Mitogen-stimulated events in nuclei of Swiss 3T3 cells. Evidence for a direct link between changes of inositol lipids, protein kinase C requirement and the onset of DNA synthesis, FEBS Lett. 283 (2) (Jun 3 1991) 243–246, https://doi.org/10.1016/0014-5793(91)80598-w (PMID: 1646120).